bioRxiv preprint doi: https://doi.org/10.1101/2020.02.14.950006; this version posted February 15, 2020. The copyright holder for this preprint (which was not certified by peer review) is the author/funder. All rights reserved. No reuse allowed without permission.

Parvalbumin$^+$ and Npas1$^+$ Pallidal Neurons Have Distinct Circuit Topology and Function

Arin Pamukcu[1], Qiaoling Cui[1], Harry S. Xenias[1], Brianna L. Berceau[1], Elizabeth C. Augustine[1], Isabel Fan[1], Adam W. Hantman[2], Talia N. Lerner[1], Simina M. Boca[3], C. Savio Chan[1]

[1] Department of Physiology, Feinberg School of Medicine, Northwestern University, Chicago, IL, USA

[2] Janelia Research Campus, Howard Hughes Medical Institute, Ashburn, VA 20147, USA

[3] Innovation Center for Biomedical Informatics, Georgetown University Medical Center, Washington D.C., USA

Correspondence should be addressed to C. Savio Chan, Department of Physiology, Feinberg School of Medicine, Northwestern University, 303 East Chicago Avenue, Chicago, IL 60611. saviochan@gmail.com

Running title: Distinct properties of GPe neuron subtype

bioRxiv preprint doi: https://doi.org/10.1101/2020.02.14.950006; this version posted February 15, 2020. The copyright holder for this preprint (which was not certified by peer review) is the author/funder. All rights reserved. No reuse allowed without permission.

Acknowledgments

This work is supported by NIH R01 NS069777 (CSC), P50 NS047085 (CSC), R01 MH112768 (CSC), R01 NS097901 (CSC), R01 MH109466 (CSC), R01 NS088528 (CSC), R00 MH109569 (TNL), DP2 MH122401 (TNL), T32 AG020506 (AP), T32 NS041234 (HSX), and F32 NS098793 (HSX). The authors would like to thank Drs. Daniel Dombeck and Geoffrey Swanson for critical feedback of the work, Dr. Kimberly Ritola for AAVretro production, Alexandria Granados, Morgan Marshall, Alyssa Bebenek, Ahana Narayanan, and Nicole Curtis, for colony management and technical assistance.

Author contributions

AP conceived the study. AP and QC designed and conducted the electrophysiological measurements. AP, QC, EA, TNL designed and conducted the behavioral experiments. HX performed pilot experiments on the anatomical properties of the STN-GPe input. AP, BLB, and IF performed histological analysis. AP and CSC wrote the manuscript with input from all co-authors. CSC designed, directed, and supervised the project. All authors reviewed and edited the manuscript.

bioRxiv preprint doi: https://doi.org/10.1101/2020.02.14.950006; this version posted February 15, 2020. The copyright holder for this preprint (which was not certified by peer review) is the author/funder. All rights reserved. No reuse allowed without permission.

Abstract (165 words)

The external globus pallidus (GPe) is a critical node within the basal ganglia circuit. Phasic changes in the activity of GPe neurons during movement and their alterations in Parkinson's disease (PD) argue that the GPe is important in motor control. PV^+ neurons and $Npas1^+$ neurons are the two principal neuron classes in the GPe. The distinct electrophysiological properties and axonal projection patterns argue that these two neuron classes serve different roles in regulating motor output. However, the causal relationship between GPe neuron classes and movement remains to be established. Here, by using optogenetic approaches, we showed that PV^+ neurons and $Npas1^+$ neurons promoted and suppressed locomotion, respectively. Moreover, PV^+ neurons and $Npas1^+$ neurons are under different synaptic influences from the subthalamic nucleus (STN). The selective weakening of STN inputs to PV^+ neurons in the chronic 6-OHDA lesion model of PD reinforces the idea that the reciprocally connected GPe-STN network plays a key role in disease symptomatology and thus provides the basis for future circuit-based therapies.

Significance Statement (118 words)

The external pallidum is a key, yet an understudied component of the basal ganglia. Neural activity in the pallidum goes awry in neurological diseases, such as Parkinson's disease. While this strongly argues that the pallidum plays a critical role in motor control, it has been difficult to establish the causal relationship between pallidal activity and motor (dys)function. This is in part due to the cellular complexity of the pallidum. Here, we showed that the two principal neuron types in the pallidum have opposing roles in motor control. In addition, we described the differences in their synaptic influence. Importantly, our research provides new insights into the cellular and circuit mechanisms that explain the hypokinetic features of Parkinson's disease.

bioRxiv preprint doi: https://doi.org/10.1101/2020.02.14.950006; this version posted February 15, 2020. The copyright holder for this preprint (which was not certified by peer review) is the author/funder. All rights reserved. No reuse allowed without permission.

Introduction (270 words)

The basal ganglia are involved in motor control and adaptive behavior [1-12]. By providing a wide projection to all structures within the basal ganglia, the external globus pallidus (GPe) is critically positioned to influence information processing within this macrocircuit [13, 14]. The classic circuit model has provided a heuristic description of motor function and dysfunction. It assumes that the GPe contains a homogeneous population of GABAergic projection neurons that act as a simple, unidirectional relay in the indirect pathway [15-21]. However, a growing body of evidence argues that the GPe is heterogeneous and serves a much more complex function [14, 22-41].

The GPe contains two principal neuron classes distinguished by their expression of the calcium-binding protein parvalbumin (PV) or the transcription factor Npas1. They account for roughly 50% and 30% of the GPe neuron population, respectively [14, 37, 38, 41-44]. PV^+ neurons and $Npas1^+$ neurons have different firing characteristics and projection targets. Specifically, PV^+ neurons exhibit higher firing rates and preferentially target the subthalamic nucleus (STN) and substantia nigra pars reticulata (SNr), whereas $Npas1^+$ neurons have lower firing rates and preferentially target the dorsal striatum (dStr) [37, 41, 42, 45, 46]. These results suggest that PV^+ neurons and $Npas1^+$ neurons likely play unique functional roles. By using the latest molecular and circuit tools, we examined the behavioral relevance and the synaptic inputs of GPe neuron subpopulations in healthy and parkinsonian mice.

Materials and Methods (2370 words)

Mice

All procedures were done in accordance with protocols approved by Northwestern University and the University of California, San Diego Institutional Animal Care and Use Committees and were in compliance with the National Institutes of Health Guide to the Care and Use of Laboratory Animals. Experiments were conducted with the following mouse lines: C57BL/6J (Jax 000664), Lox-STOP-Lox(LSL)-tdTom (Ai14, Jax 007914), Npas1-Cre-tdTom (Npas1-Cre-tdTomato BAC, Jax 027718), PV-Cre (PV-ires-Cre, Jax 017320), PV-tdTom (PV-tdTomato BAC, Jax 027395). The Npas1-Cre-tdTom BAC mouse was generated in-house [42]. PV-Cre was crossed with

bioRxiv preprint doi: https://doi.org/10.1101/2020.02.14.950006; this version posted February 15, 2020. The copyright holder for this preprint (which was not certified by peer review) is the author/funder. All rights reserved. No reuse allowed without permission.

LSL-tdTom to generate PV-L-tdTom (PV-Cre;LSL-tdTom). Only heterozygous and hemizygous mice were used throughout the study to minimize the potential alteration of the phenotypes in mice carrying the transgene alleles [47]. Mice were group-housed in a 12 h light-dark cycle. Food and water were provided *ad libitum*. All mice were maintained by backcrossing with C57BL/6J breeders (Jax 000664). The genotypes of all transgenic mice were determined by tail biopsy followed by PCR to identify the presence of the relevant transgenes. Both male and female mice were used in this study.

Stereotaxic injections

Mice aged postnatal day 30–35 were anesthetized in an isoflurane induction chamber at 3-4% isoflurane and immobilized on a stereotaxic frame (David Kopf Instruments). Anesthesia was maintained using 1-2% isoflurane. The scalp was opened using a scalpel and a small craniotomy (1 mm diameter) was made with a dental drill (Osada). Viruses were infused with calibrated 5 µl glass pipettes (VWR) pulled to have a tip diameter of 3 µm. The injection needle was left *in situ* for 5-10 min following the end of the injection to maximize tissue retention of AAV and decrease capillary spread upon pipette withdrawal. Experiments were performed 4–6 weeks after stereotaxic surgeries. The locations of the targeted injections were visually inspected under epifluorescence microscopy in *ex vivo* slices or histologically verified *post hoc*.

For *in vivo* ChR2 stimulation of PV^+ neurons or $Npas1^+$ neurons, 90 nl of AAV9.EF1a.DIO.hChR2(H134R)-eYFP.WRE was injected into the GPe of PV-Cre or Npas1-Cre-tdTom mice. Alternatively, AAV9.EF1a.DIO.rev.EYFP.WPRE.SV40pA was injected into the GPe as a viral control. For *in vivo* GtACR2 inhibition of the GPe, 90 nl of AAV1.hSyn1.SIO.stGtACR2.FusionRed was injected in the GPe of PV-Cre or Npas1-Cre-tdTom mice. For *in vivo* GtACR2 inhibition of the subthalamic nucleus (STN) or dorsal striatum (dStr), 45 nl or 720 nl of AAV1.CKIIa.stGtACR2.FusionRed was injected into the STN or dStr of C57BL/6J mice, respectively.

For *ex vivo* electrophysiological recordings of STN inputs, 45 nl of AAV.Syn.ChR2(H134R).eYFP was injected unilaterally into the STN. For CreOn expression of ChR2 in the STN, 90 nl of AAV2.retro.DIO.CAG.tdTomato was injected at the substantia nigra pars reticulata (SNr) of the LSL-tdTom mice and 45 nl of AAV9.EF1a.DIO.ChR2(H134R).eYFP into the STN. For *ex vivo* electrophysiological recordings of

bioRxiv preprint doi: https://doi.org/10.1101/2020.02.14.950006; this version posted February 15, 2020. The copyright holder for this preprint (which was not certified by peer review) is the author/funder. All rights reserved. No reuse allowed without permission.

other glutamatergic inputs, 90 nl of AAV.Syn.ChR2(H134R).eYFP was injected unilaterally into the pedunculopontine nucleus (PPN) or parafascicular nucleus of the thalamus (PF Thal). A full listing of the viral constructs and titer information is available in **Tables 1** and **2**.

Fiber implantations and behavioral testing

In naïve mice, three weeks after stereotaxic injections, a fiber optic cannula was implanted bilaterally at the region of interest (**Table 3**). Fiber cannulae with 0.63 NA, 400 μm core diameter (Prizmatix) and ceramic ferrule (Thorlabs) were prepared with non-fluorescent epoxy. Fibers that were measured to be 10 mW power at the tip were used for continuous stimulation; 15 mW power at the tip were used for 20 Hz pulse train stimulation. Cannulae were fixed to the skull using dental cement (Parkell). The locations of the targeted implantations were histologically verified *post hoc*.

Behavior tests for *in vivo* optogenetics experiments were performed in an open field box (28 cm × 28 cm) between 2:00 pm and 7:00 pm. Testing was performed in a standard lit room. Experimental boxes were cleaned with 70% ethanol prior to experimentation and before subsequent tests to remove any scent clues. Behavior tests for *in vivo* optogenetics were performed over the course of two consecutive days. On day one, each mouse was allowed to acclimate to the open-field box and the patch cord that is attached to the fiber cannula for 20 min. On day two, movement data were collected as each mouse was allowed to move freely in the open-field arena. Movement data were collected with an overhead camera and EthoVision XT (Noldus). The position of the center of the body of each mouse was used to track movement parameters and data were sampled at the maximum sampling rate of the software (10 Hz). Each mouse was allowed to acclimate for five minutes at the beginning of the behavioral session. This was followed by stimulation trials using either a continuous light pulse protocol or a pulse train (5 ms pulses at 20 Hz) protocol delivered for ten seconds with a one-minute intertrial interval. At least ten trials (60 s each) were run for any given protocol. Distance and velocity of movement were measured. The light stimulation period (referred to as “light”) corresponds to 10 s of light delivery. “Pre” and “post” periods correspond to the 10-s epoch before and after light delivery, respectively. Velocity values corresponding to pre, post, and light periods were measured by averaging the velocity during the corresponding 10 s epochs. Fold change in activity was calculated from the motor activity during “light” vs. “pre”.

bioRxiv preprint doi: https://doi.org/10.1101/2020.02.14.950006; this version posted February 15, 2020. The copyright holder for this preprint (which was not certified by peer review) is the author/funder. All rights reserved. No reuse allowed without permission.

To calculate normalized distance, data were normalized to the baseline activity measured from 25 s immediately before light. The median differences in movement velocity between "pre" and "light" and their 95% confidence intervals were estimated using the Estimation Stats application (https://www.estimationstats.com); five thousand bootstrap samples were taken; bias-corrected and accelerated (BC_a) corrections were applied to the resampling bootstrap distributions to adjust for both bias and skewness [48].

Chronic 6-OHDA lesion

To study the changes in the STN-GPe network in Parkinson's disease (PD) condition, the 6-hydroxydopamine (6-OHDA) lesion model of PD was used to achieve a chronic loss of dopamine neurons of the nigrostriatal system. Unilateral 6-OHDA lesion was achieved by injecting 6-hydroxydopamine hydrochloride (6-OHDA, 2.5 μg/μl dissolved in 0.9% w/v NaCl with 0.1% w/v ascorbic acid) into the medial forebrain bundle (**Table 2**) of the left hemisphere. Three weeks after the 6-OHDA injection, lesion success was determined by performing the cylinder task to assess forelimb use impairments. The ratio of ipsilateral to total forepaw touches was used to determine the success of lesion. In this task, during a five-minute exploratory behavioral assessment in a clear glass cylinder, weight-bearing contacts made by each forepaw on the glass walls of the cylinder were manually quantified. Forelimb use asymmetry was determined by calculating left, right, and combined forepaw touches. As impairment of the contralateral (i.e., right) forepaw was expected upon 6-OHDA lesion, a higher ratio of left to the sum of all touches indicates a more severe lesion. A ratio of 1.0 indicates that the mice only used left forelimb (ipsilateral to the lesion) for the entire test session. Mice with a ratio of forepaw touches less than 0.6 were considered poorly lesioned and were excluded from further experimental testing.

***Ex vivo* electrophysiological recordings**

Mice aged postnatal day 60–90 (4–6 weeks after AAV and 6-OHDA injections) were anesthetized with a ketamine-xylazine mixture and perfused transcardially with ice-cold artificial CSF (aCSF) containing the following (in mM): 125 NaCl, 2.5 KCl, 1.25 NaH_2PO_4, 2.0 $CaCl_2$, 1.0 $MgCl_2$, 25 $NaHCO_3$, and 12.5 glucose, bubbled continuously with carbogen (95% O_2 and 5% CO_2). The brains were rapidly removed, glued to the stage of a

bioRxiv preprint doi: https://doi.org/10.1101/2020.02.14.950006; this version posted February 15, 2020. The copyright holder for this preprint (which was not certified by peer review) is the author/funder. All rights reserved. No reuse allowed without permission.

vibrating microtome (Leica Instruments), and immersed in ice-cold aCSF. Parasagittal slices (~13°) containing the GPe were cut at a thickness of 240 µm and transferred to a holding chamber, where they were submerged in aCSF with 3.33 mM pyruvate and 0.07 mM L-glutathione at 37°C for 30 min, and brought to room temperature before recording. Slices were then transferred to a small volume (0.5 ml) Delrin recording chamber that was mounted on a fixed-stage, upright microscope (Olympus). As there is no clear demarcation between the GPe and the more ventral structures in *ex vivo* brain slices, only neurons in the dorsal two-thirds of the GPe were sampled for electrophysiological analyses. GPe neurons were visualized using differential interference contrast optics, illuminated at 735 nm (Thorlabs), and imaged with a 60× 1.0 NA water-immersion objective (Olympus) and a CCD camera (QImaging). Genetically-labeled GPe neurons were identified based on their somatic tdTomato fluorescence and examined with epifluorescence microscopy using a white (6,500 K) LED (Thorlabs) and an appropriate filter cube (Semrock). The targeting of the eYFP signal of the fused ChR2 was assessed before each recording.

Recordings were made at room temperature (20–22 °C) with patch electrodes fabricated from capillary glass (Sutter Instruments) pulled on a Flaming-Brown puller (Sutter Instruments) and fire-polished with a microforge (Narishige) immediately before use. Pipette resistance was typically 2–4 MOhms. The internal solution for cell-attached and voltage-clamp recordings of GPe neurons with STN stimulation consisted of the following (in mM): 125 $CsMeSO_3$, 5 HEPES-K, 5 EGTA-K, 10 Na_2-phosphoCreatine, 2 Mg_2ATP, 0.5 $CaCl_2$, 0.5 Na_3GTP, 0.2% (w/v) biocytin, 5 tetraethylammonium chloride , 5 QX-314 Cl. SR95531 (10 µM) and CGP55845A (1 µM) were included in the bath during recordings to block GABAergic transmission. The internal solution for anatomical analysis of STN-GPe contacts consisted of the following (in mM): 135 $KMeSO_4$, 5 KCl, 0.5 $CaCl_2$, 5 HEPES-K, 5 EGTA-K, 10 Na_2Phosphocreatine, 2 Mg_2ATP, 0.5 Na_3GTP, 0.2% (w/v) biocytin. pH was adjusted to 7.25–7.30 with KOH; osmolarity was adjusted to 290 mOsm. The liquid junction potential for this internal solution was ~6 mV and was not corrected for. Somatic patch-clamp recordings were obtained with an amplifier (Molecular Devices). The signal for all voltage-clamp recordings was filtered at 1 kHz and digitized at 10 kHz with a digitizer (Molecular Devices). For voltage-clamp recordings, series resistance was measured but not compensated for. The data were discarded if series resistance increased by 20% during recordings. Stimulus generation and data acquisition were performed using pClamp (Molecular Devices).

bioRxiv preprint doi: https://doi.org/10.1101/2020.02.14.950006; this version posted February 15, 2020. The copyright holder for this preprint (which was not certified by peer review) is the author/funder. All rights reserved. No reuse allowed without permission.

To measure the spontaneous and driven firing of GPe neurons, the cell-attached configuration was used to prevent the disruption of intracellular milieu. The average spontaneous firing was measured after 2 minutes of stable firing activity. To measure the driven firing of GPe neurons, glutamatergic neuron terminals (from STN, PF Thal, or PPN) were optogenetically stimulated with 10 ms pulses at 10 Hz for 2 seconds. The average firing rate during the 2 second stimulation period was taken as the driven firing rates of the respective cells. Whole-cell voltage-clamp recordings were used to measure excitatory postsynaptic currents (EPSCs). GPe neurons were voltage-clamped at −50 mV and STN neuron terminals were optogenetically stimulated for 10 ms. The field of illumination used for stimulation was ~500 μm in diameter. To measure STN input without the topographical biasing of the STN fibers in the GPe, recordings were made from neighboring tdTomato^{+} and tdTomato^{-} neurons (less than 150 μm apart) in both PV-L-tdTom and Npas1-Cre-tdTom mice. To study STN input with CreOn expression of ChR2, EPSC recordings were made from tdTomato^{+} and tdTomato^{-} GPe neurons in PV-L-tdTom mice. STN-GPe EPSCs were evoked by optogenetic stimulation; corticostriatal EPSCs were evoked with electrical stimulation [47]. To measure AMPA and NMDA receptor-mediated currents, the holding potential of recorded neurons was alternated between −80 mV and +40 mV. AMPA receptor-dependent currents were measured from the peak amplitude of EPCSs at −80 mV. NMDA receptor-dependent currents were measured at 50 ms after the EPSC peak at +40 mV. AMPA-NMDA ratio was calculated by dividing the AMPA current to NMDA current.

Histology

Mice aged postnatal day 55–80 were anesthetized deeply with a ketamine-xylazine mixture and perfused transcardially first with 0.01 M PBS followed by a fixative containing 4% paraformaldehyde, pH 7.4. Brain tissue was then postfixed in the same fixative for 2 h at 4°C. Tissue blocks containing the GPe were sectioned sagittally using a vibrating microtome (Leica Instruments) at a thickness of 60 μm. The sections were then washed, mounted, and coverslipped. For histological verification of infection and implantation sites in mice used for *in vivo* behavioral experiments, sections were imaged under an epifluorescence microscope (Keyence) and each section was visually inspected. For quantification of STN fibers in the GPe of naïve and 6-OHDA lesioned mice, sections were imaged with a 10× 0.45 NA (Nikon Corporation) under an epifluorescence microscope (Keyence).

bioRxiv preprint doi: https://doi.org/10.1101/2020.02.14.950006; this version posted February 15, 2020. The copyright holder for this preprint (which was not certified by peer review) is the author/funder. All rights reserved. No reuse allowed without permission.

The area of the GPe (area), percentage of pixels within the GPe due to eYFP-labeled axons (% area), and the average gray value within the pixelated area (integrated density) were quantified using Fiji (http://fiji.sc/Fiji) [49]. Brain tissue used for *ex vivo* electrophysiological recordings were stored in a 4% paraformaldehyde solution for 24 hours. PFA-fixed tissues were mounted on microscope slides, coverslipped with Prolong Gold antifade mounting medium (Invitrogen), and imaged under an epifluorescence microscope (Keyence) to inspect the fluorescent signal from the site of viral injection.

Statistical analyses

Statistical analyses were performed with MATLAB (Mathworks) and Prism (GraphPad). Custom analysis codes are available on GitHub (https://github.com/chanlab). The sample size (n value) shown represents the number of mice for *in vivo* behavior experiments and the number of cells for *ex vivo* electrophysiological experiments. No statistical method was used to predetermine the sample size. Unless noted otherwise, data are presented as median values ± median absolute deviations (MADs) as measures of central tendency and statistical dispersion, respectively. Box plots are used for graphical representation of the distribution of values [50, 51]. In a box plot, the central line represents the median, the box edges represent the interquartile ranges, and whiskers represent 10–90th percentiles. No statistical method was used to predetermine sample sizes. Comparisons for unpaired samples were performed using a Mann–Whitney U test. Comparisons for paired samples were performed using the Wilcoxon signed-rank test. Statistical significance was set at $P < 0.05$. No multiple testing corrections were considered.

Results (3178 words)

PV$^+$ neurons and Npas1$^+$ neurons play opposite roles in locomotion

We sought to dissect the relationship between GPe neuron activity and motor output with cell type-specific strategies. To confer transgene expression specificity in PV$^+$ neurons and Npas1$^+$ neurons, we used CreOn adeno-associated viruses (AAVs) in conjunction with PV-Cre and Npas1-Cre-tdTom mouse lines, respectively. *In vivo* optogenetics, which provides a relatively high temporal resolution, was used to interrogate the roles that

bioRxiv preprint doi: https://doi.org/10.1101/2020.02.14.950006; this version posted February 15, 2020. The copyright holder for this preprint (which was not certified by peer review) is the author/funder. All rights reserved. No reuse allowed without permission.

PV$^+$ neurons and Npas1$^+$ neurons play in regulating locomotor activity. Stimulation of PV$^+$ neurons *in vivo* using ChR2 (an excitatory opsin) [52] induced an increase in spontaneous movement, as measured by velocity of locomotion during open-field activity (+83.99 ± 31.49%, n = 11 mice, P = 0.00098) (**Figure 1a, Video 1**). These results were not due to phase-locking of PV$^+$ neuron activity from patterned activation of ChR2, as a sustained (10 s) light pulse was used. On the other hand, optogenetic stimulation with a 20 Hz train (10 s) was also effective in promoting motor output, arguing that the motor effects were not specific to the stimulation paradigms employed (+52.50 ± 19.52%, n = 11 mice, P = 0.00098; sustained vs train: P = 0.058). Moreover, these observations were not the result of non-specific effects of light delivery as PV-Cre mice infected with a control virus (eYFP only) did not display any motor effects with light delivery (−7.09 ± 15.48%, n = 11 mice, P = 0.46) (**Figure 1a**).

PV$^+$ neurons send inhibitory projections to the STN and SNr [13, 36, 41, 42, 45, 53]. To confirm that the movement-promoting effects of PV$^+$ neuron stimulation were mediated through inhibiting these downstream targets, we optogenetically stimulated PV$^+$ neuron axon terminals in the STN (**Figure 1b**) and SNr. As expected, stimulation of PV$^+$ axon terminals in either the STN or the SNr resulted in an increase in the velocity of movement (STN: +98 ± 20.20%, n = 6 mice, P = 0.0020; SNr: +57.72 ± 19.76%, n = 6 mice, P = 0.031). To mimic the inhibitory action of the GPe-STN input, we activated GtACR2 (an inhibitory opsin) [54] in STN neurons. As expected, we observed an increase in movement (+60.13 ± 16.42%, n = 10 mice, P = 0.0020) (**Figure 1c, Video 2**).

In contrast with the motor effects of PV$^+$ neurons, *in vivo* optogenetic stimulation of Npas1$^+$ neurons induced a decrease in movement (sustained: −35.47 ± 10.24%, n = 16 mice, P = 0.00091) (**Figure 2a, Video 3**). Optogenetic stimulation of Npas1$^+$ neurons with both a sustained light pulse and a 20 Hz-train were equally effective in suppressing motor output (train: −40.50 ± 10.09%, n = 16 mice, P = 0.00044; sustained vs train: P = 0.17). This observation is consistent with our previous findings with chemogenetic stimulation of Npas1$^+$ neurons [55]. Importantly, our observations provide a causal demonstration of the proposed role of Npas1$^+$ neurons in movement suppression [35]. On the other hand, *in vivo* optogenetic inhibition of Npas1$^+$ neurons using GtACR2 induced an increase in the movement (+34.24 ± 34.20%, n = 9 mice, P = 0.020) (**Figure 2b**). Npas1-Cre-tdTom mice infected with a control AAV (eYFP only) did not display any motor effects with light delivery (−3.80 ± 10.60%, n = 9 mice, P = 0.73) (**Figure 2a**). Npas1$^+$ neurons primarily project to the dStr [29, 37, 38, 41, 42,

bioRxiv preprint doi: https://doi.org/10.1101/2020.02.14.950006; this version posted February 15, 2020. The copyright holder for this preprint (which was not certified by peer review) is the author/funder. All rights reserved. No reuse allowed without permission.

45]. As the dStr is responsible for motor behavior [56-58], we stimulated Npas1$^+$ terminals within the dStr to determine whether the movement-suppressing effects of stimulation of Npas1$^+$ neurons are mediated through this downstream projection. Similar to the effects observed with somatic stimulation of Npas1$^+$ neurons, optogenetic stimulation of their terminals in the dStr led to a reduction in movement (−22.29 ± 12.40%, n = 10 mice, P = 0.027) (**Figure 2c**).

To confirm that the motor effects induced by optogenetic manipulation of GPe output were not a result of experimental settings unique to our experimental setup, we optogenetically stimulated direct and indirect pathway striatal projection neurons (dSPNs and iSPNs, respectively) in the dStr. This resulted in a canonical increase (+73.81 ± 21.04%, n = 8 mice, P = 0.014) and decrease (−38.61 ± 7.70%, n = 8 mice, P = 0.031) in movement, respectively, as demonstrated previously [56].

The STN target is biased toward PV$^+$ neurons

Our *in vivo* optogenetic interrogation showed that PV$^+$ neurons are movement-promoting and Npas1$^+$ neurons are movement-suppressing. However, the excitatory inputs that naturally drive the activity of these GPe neurons have not been fully characterized. Both anatomical and physiological studies show that the principal glutamatergic input to the GPe arises from the STN [59-66]. However, it is not known whether the STN selectively targets particular GPe neuron subpopulations. Computational models suggest that the STN targets a select subset of Npas1$^+$ neurons [67]; however, this hypothesis was yet to be confirmed.

To study the properties of the STN-GPe input, we performed whole-cell, voltage-clamp recordings from genetically-identified PV$^+$ neurons and Npas1$^+$ neurons in an acute brain slice preparation. To allow the stimulation of the STN input, an optogenetic approach was employed. Infection of the STN with an AAV that expressed ChR2-eYFP constitutively led to robust ChR2-eYFP expression in STN neurons, including their axons within the GPe (**Figure 3a**). In the presence of GABAergic antagonists (10 μM SR95531, 1 μM CGP55845), the properties of STN input were examined. Optogenetic stimulation of the STN input reliably evoked excitatory postsynaptic currents (EPSCs) in all neurons tested. Notably, EPSC amplitudes, as a measure of the STN input strength, were roughly five times larger in PV$^+$ neurons compared to those in Npas1$^+$ neurons (PV$^+$ = 674.01 ±

bioRxiv preprint doi: https://doi.org/10.1101/2020.02.14.950006; this version posted February 15, 2020. The copyright holder for this preprint (which was not certified by peer review) is the author/funder. All rights reserved. No reuse allowed without permission.

174.47 pA, n = 34 neurons; Npas1$^+$ = 128.30 ± 63.05 pA, n = 41 neurons; P < 0.0001) (**Figure 3b & d**). The EPSCs evoked with the constitutive ChR2 expression were not due to ectopic infection of the zona incerta (ZI), which is immediately adjacent (dorsocaudal) to the STN, as selectively-targeted infection and optogenetic stimulation of the ZI input did not produce strong EPSCs in either PV$^+$ neurons or Npas1$^+$ neurons to account for the strong biasing of STN input to PV$^+$ neurons over Npas1$^+$ neurons (PV$^+$: 33.93 ± 27.22 pA, n = 9 neurons; Npas1$^+$: 33.08 ± 20.39 pA, n = 9 neurons) (**Figure 3c, d, & e**).

As the methodology employed did not rely on an STN-specific driver or promoter, a Cre-lox strategy was used as an alternative approach to demonstrate the specificity of the involvement of the STN in our analysis. To efficiently deliver Cre to STN neurons, we injected AAV$_{retro}$-Cre [68] in the SNr, which is the principal downstream target of the STN [64, 69]. Injections of AAV$_{retro}$-Cre in the SNr of a CreOn tdTomato reporter line (LSL-tdTomato) yielded robust recombination events in STN neurons, as depicted by tdTomato expression (**Figure 3f**). PV-tdTom mice were then used in subsequent experiments to allow for the identification of GPe neurons. By using the same retrograde Cre-delivery strategy in conjunction with CreOn ChR2-expressing AAVs (injected into the STN), EPSCs were reliably evoked when STN input was optogenetically stimulated. Consistent with our observations using constitutive expression of ChR2 in the STN, EPSCs evoked with the AAV$_{retro}$-Cre-mediated strategy were larger in PV$^+$ neurons than those in PV$^-$ neurons (PV$^+$: 578.92 ± 49.01 pA, n = 6 neurons; PV$^-$: 155.64 ± 52.61 pA, n = 5 neurons; P = 0.0043). Moreover, EPSCs measured in PV$^+$ neurons and PV$^-$ neurons in mice with Cre-mediated ChR2 expression in the STN were not different than those measured in PV$^+$ neurons and Npas1$^+$ neurons in mice with constitutive ChR2 expression in the STN (PV$^+$ vs PV$^+$: P = 0.12; PV$^-$ vs Npas1$^+$: P = 0.51) (**Figure 3g**). In summary, our experiments confirmed the validity of the general approach employed in this study.

In addition to the STN, the parafascicular nucleus of the thalamus (PF Thal) and pedunculopontine nucleus (PPN) are known to send glutamatergic projections to the GPe [66, 70-75]. We sought to compare the properties of these inputs to the STN input using near-identical approaches (see **Methods**). In contrast to the STN input, not all GPe neurons responded to PF Thal or PPN input with detectable EPSCs. Fewer PV$^+$ neurons (90.6%, 19 out of 21 neurons) and Npas1$^+$ neurons (91.7%, 15 out of 17 neurons) responded to PF Thal input stimulation (PV$^+$ = 76.64 ± 44.3 pA, n = 19 neurons; Npas1$^+$ = 45.32 ± 26.9 pA, n = 15 neurons) than the STN

bioRxiv preprint doi: https://doi.org/10.1101/2020.02.14.950006; this version posted February 15, 2020. The copyright holder for this preprint (which was not certified by peer review) is the author/funder. All rights reserved. No reuse allowed without permission.

input stimulation (**Figure 3e**). Similarly, fewer PV^+ neurons (73.3%, 11 out of 15 neurons) and $Npas1^+$ neurons (54.4%, 6 out of 11 neurons) responded to PPN input stimulation (PV^+ = 54.75 ± 30.5 pA, n = 11 neurons; $Npas1^+$ = 54.32 ± 33.2 pA, n = 6 neurons) than to STN input stimulation (**Figure 3e**). Unlike the strong neuron subtype-bias in the strength of input from STN, there was no statistical difference in strength of inputs from PF Thal or PPN to the two GPe neuron subpopulations (PF Thal: n_{PV} = 19 neurons, n_{Npas1} = 15 neurons, P = 0.54; PPN: n_{PV} = 11 neurons, n_{Npas1} = 6 neurons, P = 0.35) (**Figure 3e**).

Pharmacological dissection of the synaptic responses in both PV^+ neurons and $Npas1^+$ neurons confirmed that the transmission at STN-GPe synapses was mediated by ionotropic glutamate receptors (**Figure 4a**) as suggested by earlier studies [76, 77]. Optogenetic stimulation of STN terminals in the presence of an NMDA receptor antagonist CPP (10 μM) resulted in responses with only a fast component (not shown); CPP (10 μM) and NBQX (5 μM) completely eliminated the synaptic responses. These results were consistent with prior ultrastructural studies showing that STN terminals form AMPA and NMDA receptor-containing synapses on dendrites of GPe neurons [59, 78, 79]. Our experiments collectively showed that the STN provides the primary excitatory drive to GPe neurons, and that it is unique in its cell-targeting properties.

It is established that PV^+ neurons cluster in the dorsolateral regions of the GPe [41, 42, 45, 80]. In addition, anatomical tracing studies indicate that the STN input to the GPe is topographically organized [81, 82]. It is possible that the observed differences in the measured strength of input from STN to PV^+ neurons and to $Npas1^+$ neurons were due to sampling bias across different spatial subdomains within the GPe. To this end, neighboring $tdTomato^+$ and $tdTomato^-$ neurons (less than 150 μm apart) in both PV-L-tdTom (PV-Cre;LSL-tdTom) and Npas1-Cre-tdTom mice were sampled. EPSC amplitudes in PV^+ neurons were consistently larger than those in PV^- neurons (PV^+: 674.01 ± 174.47 pA, n = 34 neurons; PV^-: 136.38 ± 60.94 pA, n = 12 neurons, P < 0.0001) (**Figure 4d**). On the other hand, $Npas1^+$ neurons had smaller EPSC amplitudes than $Npas1^-$ neurons ($Npas1^+$: 128.30 ± 63.05 pA, n = 41 neurons; $Npas1^-$: 784.82 ± 191.25 pA, n = 16 neurons; P < 0.0001) (**Figure 4d**).

bioRxiv preprint doi: https://doi.org/10.1101/2020.02.14.950006; this version posted February 15, 2020. The copyright holder for this preprint (which was not certified by peer review) is the author/funder. All rights reserved. No reuse allowed without permission.

STN-PV$^+$ input is weakened in PD

The STN-GPe network dysfunction in Parkinson's disease (PD) has been widely studied. The STN-GPe network shows abnormally synchronized oscillations in both patients and animal models of PD [83-85]. Critically, both STN lesioning and deep brain stimulation abolish these pathological oscillatory activities and have profound therapeutic benefits in alleviating the motor symptoms of PD [83, 84, 86-89]. Despite the clinical importance of the STN-GPe network, biophysical description of the alterations of the STN-GPe input in PD remains to be established. To this end, we examined the STN input to PV$^+$ neurons and Npas1$^+$ neurons in the chronic 6-OHDA lesion model of PD. Similar to the observations in naïve mice, the STN input to PV$^+$ neurons was stronger than that to Npas1$^+$ neurons in chronic 6-OHDA lesioned mice, as measured by EPSC amplitude. Importantly, STN input to PV$^+$ neurons was selectively reduced in chronic 6-OHDA lesioned mice (469.12 ± 154.33 pA, n = 36 neurons, P < 0.0001) (**Figure 4a–d, 5a & b**); this difference was observed across a range of stimulation intensities (3–106 mW/mm^2). On the contrary, STN input to Npas1$^+$ neurons did not show a detectable difference (113.28 ± 58.47 pA, n = 37 neurons, P = 0.91) (**Figure 4a–d**).

The neuronal makeup of the STN is generally thought to be homogeneous [45, 90, 91] but see [59, 92-94]. Although single axons can display target cell-specific properties [95-97], an alternative explanation for the differences in the STN input to PV$^+$ neurons and Npas1$^+$ neurons in naïve mice and their alterations in chronic 6-OHDA lesioned mice could be due to cell-specific alterations in postsynaptic receptor properties. To this end, we biophysically-isolated AMPA and NMDA receptor-dependent currents to measure their relative contribution to the synaptic responses to STN input in PV$^+$ neurons and Npas1$^+$ neurons. In addition, we compared this to a well-studied glutamatergic synapse—the corticostriatal synapse (**Figure 4e & f**). In naïve mice, both AMPA and NMDA receptor-mediated EPSCs in PV$^+$ neurons were larger than those in Npas1$^+$ neurons (AMPA current: PV$^+$ = 685.06 ± 155.03 pA, n = 22 neurons; Npas1$^+$ = 141.11 ± 45.53 pA, n = 18 neurons; P < 0.0001; NMDA current: PV$^+$ = 172.30 ± 54.26 pA, n = 22 neurons; Npas1$^+$ = 62.19 ± 38.39 pA, n = 18 neurons, P < 0.0001) (**Figure 4f & g**). The AMPA-NMDA ratio of PV$^+$ neurons was also larger than that in Npas1$^+$ neurons (PV$^+$ = 3.96 ± 0.82, n = 22 neurons; Npas1$^+$ = 1.82 ± 0.45, n = 18 neurons; P < 0.0001). The AMPA-NMDA ratio of the STN-PV$^+$ input was larger than that observed at the corticostriatal synapse (dSPN = 3.09 ± 0.40, n = 10 neurons, P = 0.014; iSPN =

bioRxiv preprint doi: https://doi.org/10.1101/2020.02.14.950006; this version posted February 15, 2020. The copyright holder for this preprint (which was not certified by peer review) is the author/funder. All rights reserved. No reuse allowed without permission.

2.14 ± 0.52, n = 16 neurons; P < 0.0001) (**Figure 4e & f**). The difference in the AMPA-NMDA ratio in PV^+ neurons and $Npas1^+$ neurons indicates that different receptor complements mediate the transmission.

Both AMPA and NMDA receptor-mediated currents in PV^+ neurons were reduced in chronic 6-OHDA lesioned mice compared to naïve mice (AMPA current = 430.79 ± 150.51 pA, n = 27 neurons, P = 0.00030; NMDA current = 116.94 ± 54.69 pA, n = 27 neurons, P = 0.024) (**Figure 4f & g**). This appeared to be a coordinated regulation, as the AMPA-NMDA ratio was unchanged in chronic 6-OHDA lesioned mice (PV^+ = 3.62 ± 0.55, n = 27 neurons, P = 0.18; $Npas1^+$ = 2.44 ± 0.71, n = 17 neurons, P = 0.68) (**Figure 4f & g**). In contrast, AMPA and NMDA receptor-mediated currents were unchanged in $Npas1^+$ neurons following chronic 6-OHDA lesion (AMPA current = 122.07 ± 52.31 pA, n = 17 neurons, P = 0.73; NMDA current = 84.35 ± 33.69 pA, n = 17 neurons, P = 0.81) (**Figure 4f & g**). These data are consistent with the downregulation of both AMPA and NMDA receptors in the GPe of PD models [98, 99]. Contrary to our prediction, we found an increase in the density of STN axonal fibers in the GPe in the chronic 6-OHDA lesioned mice (naïve = 74.84 ± 4.92%, n = 4 mice; 6-OHDA = 83.79 ± 4.56%, n = 7 mice; P = 0.0426) (**Figure 5c & d**), suggesting that rather than a reduction in the innervations from the STN, postsynaptic mechanisms were involved in the weakening of the STN input.

In light of the difference in the STN input to the two GPe neuron classes, we examined whether STN input also causes distinct changes in the activity of PV^+ neurons and $Npas1^+$ neurons. We monitored the firing of GPe neurons in response to optogenetic stimulation of the STN input. Consistent with our prior work [41, 42], PV^+ neurons and $Npas1^+$ neurons have distinct basal activity levels (PV^+: $baseline_{naïve}$ = 18.26 ± 3.74 Hz, n = 23 neurons; $Npas1^+$: $baseline_{naïve}$ = 8.91 ± 2.97 Hz, n = 10 neurons; P < 0.0001) (**Figure 6a & b**). In response to optogenetic stimulation of STN input, both PV^+ neurons and $Npas1^+$ neurons showed increases in their firing (PV^+: $stim_{naïve}$ = 51.48 ± 6.93 Hz, n = 23 neurons, P < 0.0001; $Npas1^+$: $stim_{naïve}$ = 31.68 ± 4.95 Hz, n = 10 neurons, P = 0.0020) (**Figure 6a & b**). In naïve mice, the fold change in the firing of PV^+ neurons and $Npas1^+$ neurons with STN stimulation was not significantly different ($PV^+_{naïve}$: 3.09 ± 0.90, n = 23 neurons; $Npas1^+_{naïve}$: 3.87 ± 1.13, n = 10 neurons; P = 0.48). In 6-OHDA lesion, optogenetic stimulation of STN input also resulted in increases in the firing of PV^+ neurons and $Npas1^+$ neurons (PV^+: $baseline_{6\text{-}OHDA}$ = 20.79 ± 2.97 Hz, $stim_{6\text{-}OHDA}$ = 50.49 ± 9.90 Hz, n = 15 neurons, P < 0.0001; $Npas1^+$: $baseline_{6\text{-}OHDA}$ = 5.94 ± 1.98 Hz, $stim_{6\text{-}OHDA}$ = 16.83 ± 4.95 Hz, n = 11 neurons, P = 0.0010). Consistent with a weakening of the STN-PV^+ input, PV^+ neurons showed a selective reduction in the

bioRxiv preprint doi: https://doi.org/10.1101/2020.02.14.950006; this version posted February 15, 2020. The copyright holder for this preprint (which was not certified by peer review) is the author/funder. All rights reserved. No reuse allowed without permission.

fold-increase of firing following a chronic 6-OHDA lesion (PV^+: $stim_{naïve}$ = 3.09 ± 0.90, n = 23 neurons; $stim_{6\text{-}OHDA}$ = 2.38 ± 0.27, n = 15 neurons; P = 0.0049) (**Figure 6a & b**). In contrast, $Npas1^+$ neurons did not show a change in the fold-increase in their firing between naïve and chronic 6-OHDA lesion ($Npas1^+$: $stim_{naïve}$ = 3.87 ± 1.13, n = 10 neurons; $stim_{6\text{-}OHDA}$ = 2.98 ± 0.96, n = 11 neurons; P = 0.24).

Stimulation of PV^+ neurons lessens hypokinetic symptoms

In agreement with the established relationship between STN activity and movement suppression [35, 100-103], both direct recordings and theoretical models assert that the hypokinetic symptoms of PD are a result of excessive STN activity [6, 15, 104-111]. Importantly, lesioning and inactivation studies from animal models of PD further support this idea [112, 113] but see [114]. In other words, the weakening of the STN-PV^+ input that we observed in the chronic 6-OHDA lesioned mice *ex vivo* can thus be a form of homeostatic scaling in response to the increased excitatory drive. However, this alteration may, in fact, be maladaptive as it would lead to decreased GPe feedback and thus disinhibition of the STN. If our interpretation is correct, then optogenetic stimulation of PV^+ neurons should restore motor activity in chronic 6-OHDA lesioned mice. Chronic 6-OHDA lesioned mice have reduced motor activity ($naïve_{baseline}$ = 2.74 ± 0.30 cm/s, n = 11 mice; $6\text{-}OHDA_{baseline}$ = 1.42 ± 0.43 cm/s, n = 13 mice, P = 0.0073), as expected. Under this condition, ChR2-mediated stimulation of PV^+ neurons increased locomotion in chronic 6-OHDA mice; the extent of the increase was comparable to that observed in naïve mice (83.69 ± 26.38%, n =13 mice, P = 0.70) (**Figure 7a**). Moreover, stimulation of PV^+ neurons in 6-OHDA mice restored motor activity to the level as the baseline activity in naïve mice ($naïve_{baseline}$ = 2.74 ± 0.30 cm/s, n = 11 mice; $6\text{-}OHDA_{light}$ = 2.62 ± 0.70 cm/s, n = 13 mice, P = 0.17).

Discussion (1484 words)

Recent studies have shown that PV^+ neurons and $Npas1^+$ neurons in the GPe form two near-exclusive, principal neuron classes that display molecular, electrophysiological, and anatomical dichotomy [14, 41-44]. These findings led us to hypothesize that PV^+ neurons and $Npas1^+$ neurons are embedded in distinct circuits. In this study, by optogenetically manipulating the activity of specific GPe neuron subpopulations and their downstream

bioRxiv preprint doi: https://doi.org/10.1101/2020.02.14.950006; this version posted February 15, 2020. The copyright holder for this preprint (which was not certified by peer review) is the author/funder. All rights reserved. No reuse allowed without permission.

targets, we concluded that PV$^+$ neurons are movement-promoting and Npas1$^+$ neurons are movement-inhibiting.

GPe neuron subtypes have opposing roles in motor control

Early studies showed that GPe neurons change their activity in relation to movement; however, the identity of the recorded neurons was unknown [11, 19, 22-25, 35, 115-120]. Yoshida et al. observed two types of neurons; decrease-type and increase-type neurons that they defined by the direction of change in their firing in response to antisaccade movements [39]. More recent studies suggest that GPe neuron subtypes show changes in their activity during spontaneous body movements [38]. Moreover, a time-locked increase in the activity of a subset of Npas1$^+$ neurons correlated with the disruption of movement [121]. Here, our data along with our previous study demonstrate the causality between the activity of Npas1$^+$ neurons and motor output [55].

Our current data show that in naïve mice, stimulation of PV$^+$ neurons and their terminals in the STN and SNr promoted movement. To our knowledge, this has not been previously reported. Though in acute dopamine-depleted mice, repetitive PV$^+$ neuron stimulation was shown to persistently restore mobility [46], we did not observe a persistent behavioral effect in our chronic lesion model of PD. Consistent with the fact that STN neuron activity is associated with movement inhibition [35, 100-103, 122], here, we showed that phasic inhibition of STN neurons is movement-promoting. In addition, as the GABAergic projection from PV$^+$ neurons to the SNr is also movement-promoting, this PV$^+$-SNr projection further reinforces the movement promotion imposed by the PV$^+$-STN projection. Although our observation is in line with the findings from our lab and others [55, 121], we do not fully understand the motor suppression produced by Npas1$^+$ neurons. Although Npas1$^+$ neurons have extensive axonal arborization in the dStr, their inhibition on somatic spikes is relatively weak [55]. It is possible that additional signaling partners are involved.

In this study, we drove the activity of PV$^+$ neurons or Npas1$^+$ neurons by activating ChR2. These experiments were critical to establishing the causal role of PV$^+$ neurons and Npas1$^+$ neurons in motor control. By directing light stimulus to different brain structures, we dissected the circuit elements that are involved in these motor effects. While these gain-of-function experiments caused observable motor effects, they are

bioRxiv preprint doi: https://doi.org/10.1101/2020.02.14.950006; this version posted February 15, 2020. The copyright holder for this preprint (which was not certified by peer review) is the author/funder. All rights reserved. No reuse allowed without permission.

insufficient to conclude if the motor effects are the native functions mediated by PV$^+$ neurons and Npas1$^+$ neurons. We addressed this by performing loss-of-function experiments using GtCAR2 to inhibit GPe neuron subtypes or their postsynaptic targets. GPe neurons are known to form intranuclear collaterals [33, 123-125]. As we do not yet have the tools for the selective manipulation of these local collaterals, we will need to rely on *ex vivo* studies to assess their relevance based on the connectivity principle of these local connections. In sum, our *in vivo* studies reinforce the notion from prior *in vivo* electrophysiological studies that GPe neurons are critical for movement. Importantly, we have now identified the circuit elements involved.

There are a number of possible explanations for the biological significance of PV$^+$ neurons and Npas1$^+$ neurons. It is conceivable that the two neuron populations with opposing functions form a rheostat in controlling net motor output. On the other hand, as both initiation and termination of motor programs are equally important [4, 5], it is possible that PV$^+$ neurons and Npas1$^+$ neurons are differentially involved in selecting voluntary versus suppressing competing motor programs. Alternatively, GPe neuron subtypes can be selectively engaged in the regulation of antagonistic muscle groups that are necessary for the execution of one specific movement. Similar ideas have been proposed for striatal neurons [8, 126-128]. To gain new insights into this topic, it will be important in the future to determine the temporal organization of the activity of GPe neuron subtypes in relation to movement.

STN preferentially target PV$^+$ neurons

In this study, we found that the STN provides a stronger input to PV$^+$ neurons than to Npas1$^+$ neurons. Our finding contrasts with computational studies that predicted a stronger connection from the STN to a subset of Npas1$^+$ neurons [67]. As we found a notable input from the STN to Npas1$^+$ neurons, it is possible that the STN input regulates movement via sending an efferent copy to the Npas1$^+$ neurons in addition to the primary projection to its downstream target, i.e., PV$^+$ neurons. Moreover, the difference in the AMPA-NMDA ratio of the synaptic responses in PV$^+$ neurons and Npas1$^+$ neurons indicates that the STN input to these neurons is mediated by different complements in the postsynaptic glutamate receptors. On the other hand, recent studies indicate the presence of heterogeneity in STN neurons [59, 92-94, 129]. It is possible that unique STN neurons provide inputs to distinct GPe neuron subpopulations. As we are only beginning to grasp the cellular

bioRxiv preprint doi: https://doi.org/10.1101/2020.02.14.950006; this version posted February 15, 2020. The copyright holder for this preprint (which was not certified by peer review) is the author/funder. All rights reserved. No reuse allowed without permission.

heterogeneity within both the GPe and STN, additional work is needed to further our understanding of the organization of the STN-GPe network. As PV^+ neurons form the principal inhibitory innervation to the STN [36, 37, 42, 45], these data collectively demonstrate a closed reciprocal feedback loop formed between the STN and PV^+ neurons. Although earlier studies have examined the electrophysiological and anatomical properties of STN-GPe network [13, 36, 37, 42, 45, 62, 66, 76, 130, 131], the cell-type specificity of the STN input in the GPe was not known. Importantly, our new data added critical insights into the cellular constituents that are involved in this reciprocal loop.

We found that in addition to the STN, the PF Thal and PPN provide excitatory inputs to the GPe. However, our *ex vivo* data showed that not all GPe neurons responded to the stimulation of PF Thal and PPN inputs. This heterogeneity existed in both PV^+ neurons and $Npas1^+$ neurons. Although it is possible that inputs from PF Thal and PPN target specific subpopulations of GPe neurons, a systematic examination will be required to test if the observed heterogeneity correlates with the expression of subclass-specific molecular markers in GPe neurons. In addition, we, and others, have shown that the cortex is another major source of excitatory input to the GPe [41, 53, 77, 132, 133]. However, the properties of this input remain to be fully characterized. It will be important to further examine the properties of the corticopallidal projection, including their alterations in models of PD.

The STN-GPe network is important in health and in PD

In this study, we found that the STN input to PV^+ neurons is reduced in chronic 6-OHDA lesioned mice. These findings are consistent with the downregulation of AMPA and NMDA receptors in the GPe of PD models [98, 99]. We have previously found a decrease in the ambient glutamate content in the GPe following a chronic loss of dopamine [134]; our current study adds to the literature that glutamatergic signaling in the GPe is altered in PD.

STN-GPe network function and its dysfunction in the context of PD have been widely studied. Experimental and computational studies suggest that the STN-GPe network acts as an intrinsic oscillator [135-138]. Abnormally synchronized beta oscillations (i.e., 15–30 Hz) in the STN-GPe network are thought to be partially responsible for the hypokinetic symptoms of PD [15, 84, 108, 139]. Abolishing the pathological oscillatory activity by lesioning or deep-brain stimulation of the STN or the GPe has profound therapeutic

bioRxiv preprint doi: https://doi.org/10.1101/2020.02.14.950006; this version posted February 15, 2020. The copyright holder for this preprint (which was not certified by peer review) is the author/funder. All rights reserved. No reuse allowed without permission.

benefits in alleviating motor symptoms of PD [86-88]. We previously observed strengthening of the GABAergic GPe input to the STN with chronic 6-OHDA lesion [140]; it is now clear that this input arises from PV^+ neurons as PV^+ neurons are the primary source of inhibitory input to the STN [36, 41, 42]. As the activity of the STN negatively regulates motor output [35, 100, 101], a decrease in the ambient glutamate content in the GPe [134], along with a reduction in the STN-PV^+ input, would disinhibit the STN and suppress motor output in the parkinsonian state, thus explaining the hypokinetic symptoms of PD. On the other hand, a strengthening of the inhibitory PV^+ input to the STN [141] would promote movement and may act as a compensatory mechanism against the hypokinetic effects of the abnormal glutamatergic signaling in the GPe in PD. How these synaptic adaptations interact and impact pathological, correlated activity patterns in the STN-GPe is yet to be fully understood [142]. In the future, it will be important to understand the exact mechanism through which dopamine loss results in the cellular alterations in the STN-GPe network.

bioRxiv preprint doi: https://doi.org/10.1101/2020.02.14.950006; this version posted February 15, 2020. The copyright holder for this preprint (which was not certified by peer review) is the author/funder. All rights reserved. No reuse allowed without permission.

References

1. Cox, J. and I.B. Witten, *Striatal circuits for reward learning and decision-making.* Nat Rev Neurosci, 2019. **20**(8): p. 482-494.
2. Pennartz, C.M., et al., *Corticostriatal Interactions during Learning, Memory Processing, and Decision Making.* J Neurosci, 2009. **29**(41): p. 12831-8.
3. Dudman, J.T. and J.W. Krakauer, *The basal ganglia: from motor commands to the control of vigor.* Curr Opin Neurobiol, 2016. **37**: p. 158-166.
4. Redgrave, P., et al., *Goal-directed and habitual control in the basal ganglia: implications for Parkinson's disease.* Nat Rev Neurosci, 2010. **11**(11): p. 760-72.
5. Jahanshahi, M., et al., *A fronto-striato-subthalamic-pallidal network for goal-directed and habitual inhibition.* Nat Rev Neurosci, 2015. **16**(12): p. 719-32.
6. DeLong, M.R. and T. Wichmann, *Circuits and circuit disorders of the basal ganglia.* Arch Neurol, 2007. **64**(1): p. 20-4.
7. Nambu, A. and Y. Tachibana, *Mechanism of parkinsonian neuronal oscillations in the primate basal ganglia: some considerations based on our recent work.* Front Syst Neurosci, 2014. **8**: p. 74.
8. Klaus, A., J. Alves da Silva, and R.M. Costa, *What, If, and When to Move: Basal Ganglia Circuits and Self-Paced Action Initiation.* Annu Rev Neurosci, 2019. **42**: p. 459-483.
9. Graybiel, A.M., *Habits, rituals, and the evaluative brain.* Annu Rev Neurosci, 2008. **31**: p. 359-87.
10. Mink, J.W., *Basal ganglia mechanisms in action selection, plasticity, and dystonia.* Eur J Paediatr Neurol, 2018. **22**(2): p. 225-229.
11. Mink, J.W. and W.T. Thach, *Basal ganglia motor control. I. Nonexclusive relation of pallidal discharge to five movement modes.* J Neurophysiol, 1991. **65**(2): p. 273-300.
12. Ito, M. and K. Doya, *Multiple representations and algorithms for reinforcement learning in the cortico-basal ganglia circuit.* Curr Opin Neurobiol, 2011. **21**(3): p. 368-73.
13. Kita, H., *Globus pallidus external segment.* Prog Brain Res, 2007. **160**: p. 111-33.
14. Hegeman, D.J., et al., *The external globus pallidus: progress and perspectives.* Eur J Neurosci, 2016. **43**(10): p. 1239-65.

bioRxiv preprint doi: https://doi.org/10.1101/2020.02.14.950006; this version posted February 15, 2020. The copyright holder for this preprint (which was not certified by peer review) is the author/funder. All rights reserved. No reuse allowed without permission.

15. Albin, R.L., A.B. Young, and J.B. Penney, *The functional anatomy of basal ganglia disorders.* Trends Neurosci, 1989. **12**(10): p. 366-75.

16. Albin, R.L., A.B. Young, and J.B. Penney, *The functional anatomy of disorders of the basal ganglia.* Trends Neurosci, 1995. **18**(2): p. 63-4.

17. Alexander, G.E. and M.D. Crutcher, *Functional architecture of basal ganglia circuits: neural substrates of parallel processing.* Trends Neurosci, 1990. **13**(7): p. 266-71.

18. DeLong, M.R., *Primate models of movement disorders of basal ganglia origin.* Trends Neurosci, 1990. **13**(7): p. 281-5.

19. Parent, A. and L.N. Hazrati, *Functional anatomy of the basal ganglia. II. The place of subthalamic nucleus and external pallidum in basal ganglia circuitry.* Brain Res Brain Res Rev, 1995. **20**(1): p. 128-54.

20. Joel, D. and I. Weiner, *The connections of the primate subthalamic nucleus: indirect pathways and the open-interconnected scheme of basal ganglia-thalamocortical circuitry.* Brain Res Brain Res Rev, 1997. **23**(1-2): p. 62-78.

21. Graybiel, A.M., *The basal ganglia.* Curr Biol, 2000. **10**(14): p. R509-11.

22. Anderson, M.E. and F.B. Horak, *Influence of the globus pallidus on arm movements in monkeys. III. Timing of movement-related information.* J Neurophysiol, 1985. **54**(2): p. 433-48.

23. DeLong, M.R., *Activity of pallidal neurons during movement.* J Neurophysiol, 1971. **34**(3): p. 414-27.

24. Mink, J.W. and W.T. Thach, *Basal ganglia motor control. II. Late pallidal timing relative to movement onset and inconsistent pallidal coding of movement parameters.* J Neurophysiol, 1991. **65**(2): p. 301-29.

25. Mitchell, S.J., et al., *The primate globus pallidus: neuronal activity related to direction of movement.* Exp Brain Res, 1987. **68**(3): p. 491-505.

26. Nambu, A. and R. Llinas, *Electrophysiology of globus pallidus neurons in vitro.* J Neurophysiol, 1994. **72**(3): p. 1127-39.

27. Kelland, M.D., et al., *In vivo characterization of two cell types in the rat globus pallidus which have opposite responses to dopamine receptor stimulation: comparison of electrophysiological properties and responses to apomorphine, dizocilpine, and ketamine anesthesia.* Synapse, 1995. **20**(4): p. 338-50.

bioRxiv preprint doi: https://doi.org/10.1101/2020.02.14.950006; this version posted February 15, 2020. The copyright holder for this preprint (which was not certified by peer review) is the author/funder. All rights reserved. No reuse allowed without permission.

28. Bevan, M.D., et al., *Selective innervation of neostriatal interneurons by a subclass of neuron in the globus pallidus of the rat.* J Neurosci, 1998. **18**(22): p. 9438-52.

29. Kita, H., H. Tokuno, and A. Nambu, *Monkey globus pallidus external segment neurons projecting to the neostriatum.* Neuroreport, 1999. **10**(7): p. 1467-72.

30. Cooper, A.J. and I.M. Stanford, *Electrophysiological and morphological characteristics of three subtypes of rat globus pallidus neurone in vitro.* J Physiol, 2000. **527 Pt 2**: p. 291-304.

31. Gunay, C., J.R. Edgerton, and D. Jaeger, *Channel density distributions explain spiking variability in the globus pallidus: a combined physiology and computer simulation database approach.* J Neurosci, 2008. **28**(30): p. 7476-91.

32. Mallet, N., et al., *Parkinsonian beta oscillations in the external globus pallidus and their relationship with subthalamic nucleus activity.* J Neurosci, 2008. **28**(52): p. 14245-58.

33. Mallet, N., et al., *Dichotomous organization of the external globus pallidus.* Neuron, 2012. **74**(6): p. 1075-86.

34. Chuhma, N., et al., *Functional connectome of the striatal medium spiny neuron.* J Neurosci, 2011. **31**(4): p. 1183-92.

35. Schmidt, R., et al., *Canceling actions involves a race between basal ganglia pathways.* Nat Neurosci, 2013. **16**(8): p. 1118-24.

36. Mastro, K.J., et al., *Transgenic mouse lines subdivide external segment of the globus pallidus (GPe) neurons and reveal distinct GPe output pathways.* J Neurosci, 2014. **34**(6): p. 2087-99.

37. Abdi, A., et al., *Prototypic and arkypallidal neurons in the dopamine-intact external globus pallidus.* J Neurosci, 2015. **35**(17): p. 6667-88.

38. Dodson, P.D., et al., *Distinct developmental origins manifest in the specialized encoding of movement by adult neurons of the external globus pallidus.* Neuron, 2015. **86**(2): p. 501-13.

39. Yoshida, A. and M. Tanaka, *Two Types of Neurons in the Primate Globus Pallidus External Segment Play Distinct Roles in Antisaccade Generation.* Cereb Cortex, 2016. **26**(3): p. 1187-99.

40. Hunt, A.J., Jr., et al., *Paraventricular hypothalamic and amygdalar CRF neurons synapse in the external globus pallidus.* Brain Struct Funct, 2018. **223**(6): p. 2685-2698.

bioRxiv preprint doi: https://doi.org/10.1101/2020.02.14.950006; this version posted February 15, 2020. The copyright holder for this preprint (which was not certified by peer review) is the author/funder. All rights reserved. No reuse allowed without permission.

41. Abecassis, Z.A., et al., *Npas1(+)-Nkx2.1(+) Neurons Are an Integral Part of the Cortico-pallido-cortical Loop.* J Neurosci, 2020. **40**(4): p. 743-768.

42. Hernandez, V.M., et al., *Parvalbumin+ Neurons and Npas1+ Neurons Are Distinct Neuron Classes in the Mouse External Globus Pallidus.* J Neurosci, 2015. **35**(34): p. 11830-47.

43. Nobrega-Pereira, S., et al., *Origin and molecular specification of globus pallidus neurons.* J Neurosci, 2010. **30**(8): p. 2824-34.

44. Flandin, P., S. Kimura, and J.L. Rubenstein, *The progenitor zone of the ventral medial ganglionic eminence requires Nkx2-1 to generate most of the globus pallidus but few neocortical interneurons.* J Neurosci, 2010. **30**(8): p. 2812-23.

45. Saunders, A., K.W. Huang, and B.L. Sabatini, *Globus Pallidus Externus Neurons Expressing parvalbumin Interconnect the Subthalamic Nucleus and Striatal Interneurons.* PLoS One, 2016. **11**(2): p. e0149798.

46. Mastro, K.J., et al., *Cell-specific pallidal intervention induces long-lasting motor recovery in dopamine-depleted mice.* Nat Neurosci, 2017. **20**(6): p. 815-823.

47. Chan, C.S., et al., *Strain-specific regulation of striatal phenotype in Drd2-eGFP BAC transgenic mice.* J Neurosci, 2012. **32**(27): p. 9124-32.

48. Ho, J., et al., *Moving beyond P values: data analysis with estimation graphics.* Nat Methods, 2019. **16**(7): p. 565-566.

49. Schindelin, J., et al., *Fiji: an open-source platform for biological-image analysis.* Nat Methods, 2012. **9**(7): p. 676-82.

50. Krzywinski, M. and N. Altman, *Visualizing samples with box plots.* Nat Methods, 2014. **11**(2): p. 119-20.

51. Streit, M. and N. Gehlenborg, *Bar charts and box plots.* Nat Methods, 2014. **11**(2): p. 117.

52. Boyden, E.S., et al., *Millisecond-timescale, genetically targeted optical control of neural activity.* Nat Neurosci, 2005. **8**(9): p. 1263-8.

53. Fujiyama, F., et al., *A single-neuron tracing study of arkypallidal and prototypic neurons in healthy rats.* Brain Struct Funct, 2016. **221**(9): p. 4733-4740.

54. Mahn, M., et al., *High-efficiency optogenetic silencing with soma-targeted anion-conducting channelrhodopsins.* Nat Commun, 2018. **9**(1): p. 4125.

bioRxiv preprint doi: https://doi.org/10.1101/2020.02.14.950006; this version posted February 15, 2020. The copyright holder for this preprint (which was not certified by peer review) is the author/funder. All rights reserved. No reuse allowed without permission.

55. Glajch, K.E., et al., *Npas1+ Pallidal Neurons Target Striatal Projection Neurons.* J Neurosci, 2016. **36**(20): p. 5472-88.

56. Kravitz, A.V., et al., *Regulation of parkinsonian motor behaviours by optogenetic control of basal ganglia circuitry.* Nature, 2010. **466**(7306): p. 622-6.

57. Freeze, B.S., et al., *Control of basal ganglia output by direct and indirect pathway projection neurons.* J Neurosci, 2013. **33**(47): p. 18531-9.

58. Durieux, P.F., S.N. Schiffmann, and A. de Kerchove d'Exaerde, *Differential regulation of motor control and response to dopaminergic drugs by D1R and D2R neurons in distinct dorsal striatum subregions.* EMBO J, 2012. **31**(3): p. 640-53.

59. Koshimizu, Y., et al., *Quantitative analysis of axon bouton distribution of subthalamic nucleus neurons in the rat by single neuron visualization with a viral vector.* J Comp Neurol, 2013. **521**(9): p. 2125-46.

60. Carpenter, M.B., et al., *Interconnections and organization of pallidal and subthalamic nucleus neurons in the monkey.* J Comp Neurol, 1981. **197**(4): p. 579-603.

61. Carpenter, M.B., et al., *Connections of the subthalamic nucleus in the monkey.* Brain Res, 1981. **224**(1): p. 1-29.

62. Kita, H. and S.T. Kitai, *Efferent projections of the subthalamic nucleus in the rat: light and electron microscopic analysis with the PHA-L method.* J Comp Neurol, 1987. **260**(3): p. 435-52.

63. Smith, Y., J.P. Bolam, and M. Von Krosigk, *Topographical and Synaptic Organization of the GABA-Containing Pallidosubthalamic Projection in the Rat.* Eur J Neurosci, 1990. **2**(6): p. 500-511.

64. Smith, Y., et al., *Microcircuitry of the direct and indirect pathways of the basal ganglia.* Neuroscience, 1998. **86**(2): p. 353-87.

65. Smith, Y., L.N. Hazrati, and A. Parent, *Efferent projections of the subthalamic nucleus in the squirrel monkey as studied by the PHA-L anterograde tracing method.* J Comp Neurol, 1990. **294**(2): p. 306-23.

66. Kita, H., et al., *Role of ionotropic glutamatergic and GABAergic inputs on the firing activity of neurons in the external pallidum in awake monkeys.* J Neurophysiol, 2004. **92**(5): p. 3069-84.

67. Bogacz, R., et al., *Properties of Neurons in External Globus Pallidus Can Support Optimal Action Selection.* PLoS Comput Biol, 2016. **12**(7): p. e1005004.

bioRxiv preprint doi: https://doi.org/10.1101/2020.02.14.950006; this version posted February 15, 2020. The copyright holder for this preprint (which was not certified by peer review) is the author/funder. All rights reserved. No reuse allowed without permission.

68. Tervo, D.G., et al., *A Designer AAV Variant Permits Efficient Retrograde Access to Projection Neurons.* Neuron, 2016. **92**(2): p. 372-382.

69. Parent, A. and Y. Smith, *Organization of efferent projections of the subthalamic nucleus in the squirrel monkey as revealed by retrograde labeling methods.* Brain Res, 1987. **436**(2): p. 296-310.

70. Deschenes, M., et al., *A single-cell study of the axonal projections arising from the posterior intralaminar thalamic nuclei in the rat.* Eur J Neurosci, 1996. **8**(2): p. 329-43.

71. Kincaid, A.E., et al., *Evidence for a projection from the globus pallidus to the entopeduncular nucleus in the rat.* Neurosci Lett, 1991. **128**(1): p. 121-5.

72. Mouroux, M., O.K. Hassani, and J. Feger, *Electrophysiological and Fos immunohistochemical evidence for the excitatory nature of the parafascicular projection to the globus pallidus.* Neuroscience, 1997. **81**(2): p. 387-97.

73. Naito, A. and H. Kita, *The cortico-pallidal projection in the rat: an anterograde tracing study with biotinylated dextran amine.* Brain Res, 1994. **653**(1-2): p. 251-7.

74. Sadikot, A.F., et al., *Efferent connections of the centromedian and parafascicular thalamic nuclei in the squirrel monkey: a light and electron microscopic study of the thalamostriatal projection in relation to striatal heterogeneity.* J Comp Neurol, 1992. **320**(2): p. 228-42.

75. Yasukawa, T., et al., *Rat intralaminar thalamic nuclei projections to the globus pallidus: a biotinylated dextran amine anterograde tracing study.* J Comp Neurol, 2004. **471**(2): p. 153-67.

76. Kita, H. and S.T. Kitai, *Intracellular study of rat globus pallidus neurons: membrane properties and responses to neostriatal, subthalamic and nigral stimulation.* Brain Res, 1991. **564**(2): p. 296-305.

77. Kita, H., *Responses of globus pallidus neurons to cortical stimulation: intracellular study in the rat.* Brain Res, 1992. **589**(1): p. 84-90.

78. Clarke, N.P. and J.P. Bolam, *Distribution of glutamate receptor subunits at neurochemically characterized synapses in the entopeduncular nucleus and subthalamic nucleus of the rat.* J Comp Neurol, 1998. **397**(3): p. 403-20.

bioRxiv preprint doi: https://doi.org/10.1101/2020.02.14.950006; this version posted February 15, 2020. The copyright holder for this preprint (which was not certified by peer review) is the author/funder. All rights reserved. No reuse allowed without permission.

79. Bernard, V. and J.P. Bolam, *Subcellular and subsynaptic distribution of the NR1 subunit of the NMDA receptor in the neostriatum and globus pallidus of the rat: co-localization at synapses with the GluR2/3 subunit of the AMPA receptor.* Eur J Neurosci, 1998. **10**(12): p. 3721-36.

80. Karube, F., et al., *Motor cortex can directly drive the globus pallidus neurons in a projection neuron type-dependent manner in the rat.* Elife, 2019. **8**.

81. Iwamuro, H., *Electrophysiological evidences of organization of cortical motor information in the Basal Ganglia.* J Mov Disord, 2011. **4**(1): p. 8-12.

82. Nambu, A., *Somatotopic organization of the primate Basal Ganglia.* Front Neuroanat, 2011. **5**: p. 26.

83. Brown, P., *Bad oscillations in Parkinson's disease.* J Neural Transm Suppl, 2006(70): p. 27-30.

84. Hurtado, J.M., et al., *Dynamics of tremor-related oscillations in the human globus pallidus: a single case study.* Proc Natl Acad Sci U S A, 1999. **96**(4): p. 1674-9.

85. Plenz, D. and S.T. Kital, *A basal ganglia pacemaker formed by the subthalamic nucleus and external globus pallidus.* Nature, 1999. **400**(6745): p. 677-82.

86. Vitek, J.L., et al., *External pallidal stimulation improves parkinsonian motor signs and modulates neuronal activity throughout the basal ganglia thalamic network.* Exp Neurol, 2012. **233**(1): p. 581-6.

87. Kuhn, A.A., et al., *Reduction in subthalamic 8-35 Hz oscillatory activity correlates with clinical improvement in Parkinson's disease.* Eur J Neurosci, 2006. **23**(7): p. 1956-60.

88. Bergman, H., T. Wichmann, and M.R. DeLong, *Reversal of experimental parkinsonism by lesions of the subthalamic nucleus.* Science, 1990. **249**(4975): p. 1436-8.

89. Vitek, J.L., et al., *Acute stimulation in the external segment of the globus pallidus improves parkinsonian motor signs.* Mov Disord, 2004. **19**(8): p. 907-15.

90. Yelnik, J. and G. Percheron, *Subthalamic neurons in primates: a quantitative and comparative analysis.* Neuroscience, 1979. **4**(11): p. 1717-43.

91. Hammond, C. and J. Yelnik, *Intracellular labelling of rat subthalamic neurones with horseradish peroxidase: computer analysis of dendrites and characterization of axon arborization.* Neuroscience, 1983. **8**(4): p. 781-90.

bioRxiv preprint doi: https://doi.org/10.1101/2020.02.14.950006; this version posted February 15, 2020. The copyright holder for this preprint (which was not certified by peer review) is the author/funder. All rights reserved. No reuse allowed without permission.

92. Xiao, C., et al., *Nicotinic receptor subtype-selective circuit patterns in the subthalamic nucleus.* J Neurosci, 2015. **35**(9): p. 3734-46.

93. Sato, F., et al., *Axonal branching pattern of neurons of the subthalamic nucleus in primates.* J Comp Neurol, 2000. **424**(1): p. 142-52.

94. Papathanou, M., et al., *Single-nuclei transcriptomic analysis of the subthalamic nucleus reveals different Pitx2-positive subpopulations.* bioRxiv, 2019: p. 677724.

95. Shigemoto, R., et al., *Target-cell-specific concentration of a metabotropic glutamate receptor in the presynaptic active zone.* Nature, 1996. **381**(6582): p. 523-5.

96. Sun, H.Y., et al., *Target-cell-specific Short-term Plasticity Reduces the Excitatory Drive onto CA1 Interneurons Relative to Pyramidal Cells During Physiologically-derived Spike Trains.* Neuroscience, 2018. **388**: p. 430-447.

97. Patel, A.B., et al., *A target cell-specific role for presynaptic Fmr1 in regulating glutamate release onto neocortical fast-spiking inhibitory neurons.* J Neurosci, 2013. **33**(6): p. 2593-604.

98. Porter, R.H., et al., *Polysynaptic regulation of glutamate receptors and mitochondrial enzyme activities in the basal ganglia of rats with unilateral dopamine depletion.* J Neurosci, 1994. **14**(11 Pt 2): p. 7192-9.

99. Betarbet, R., R.H. Porter, and J.T. Greenamyre, *GluR1 glutamate receptor subunit is regulated differentially in the primate basal ganglia following nigrostriatal dopamine denervation.* J Neurochem, 2000. **74**(3): p. 1166-74.

100. Fife, K.H., et al., *Causal role for the subthalamic nucleus in interrupting behavior.* Elife, 2017. **6**.

101. Wessel, J.R. and A.R. Aron, *On the Globality of Motor Suppression: Unexpected Events and Their Influence on Behavior and Cognition.* Neuron, 2017. **93**(2): p. 259-280.

102. Hamani, C., et al., *The subthalamic nucleus in the context of movement disorders.* Brain, 2004. **127**(Pt 1): p. 4-20.

103. Adam, E.M., T. Johns, and M. Sur, *Cortico-subthalamic projections send brief stop signals to halt visually-guided locomotion.* bioRxiv, 2020: p. 2020.02.05.936443.

104. Bergman, H., et al., *The primate subthalamic nucleus. II. Neuronal activity in the MPTP model of parkinsonism.* J Neurophysiol, 1994. **72**(2): p. 507-20.

bioRxiv preprint doi: https://doi.org/10.1101/2020.02.14.950006; this version posted February 15, 2020. The copyright holder for this preprint (which was not certified by peer review) is the author/funder. All rights reserved. No reuse allowed without permission.

105. Zaidel, A., et al., *Akineto-rigid vs. tremor syndromes in Parkinsonism.* Curr Opin Neurol, 2009. **22**(4): p. 387-93.

106. Sharott, A., et al., *Activity parameters of subthalamic nucleus neurons selectively predict motor symptom severity in Parkinson's disease.* J Neurosci, 2014. **34**(18): p. 6273-85.

107. Obeso, J.A., et al., *Pathophysiology of the basal ganglia in Parkinson's disease.* Trends Neurosci, 2000. **23**(10 Suppl): p. S8-19.

108. McGregor, M.M. and A.B. Nelson, *Circuit Mechanisms of Parkinson's Disease.* Neuron, 2019. **101**(6): p. 1042-1056.

109. DeLong, M.R. and T. Wichmann, *Basal Ganglia Circuits as Targets for Neuromodulation in Parkinson Disease.* JAMA Neurol, 2015. **72**(11): p. 1354-60.

110. Bergman, H., et al., *Physiological aspects of information processing in the basal ganglia of normal and parkinsonian primates.* Trends Neurosci, 1998. **21**(1): p. 32-8.

111. Wichmann, T. and M.R. DeLong, *Functional and pathophysiological models of the basal ganglia.* Curr Opin Neurobiol, 1996. **6**(6): p. 751-8.

112. Levy, R., et al., *Lidocaine and muscimol microinjections in subthalamic nucleus reverse Parkinsonian symptoms.* Brain, 2001. **124**(Pt 10): p. 2105-18.

113. Yoon, H.H., et al., *Optogenetic inactivation of the subthalamic nucleus improves forelimb akinesia in a rat model of Parkinson disease.* Neurosurgery, 2014. **74**(5): p. 533-40; discussion 540-1.

114. McIver, E.L., et al., *Maladaptive Downregulation of Autonomous Subthalamic Nucleus Activity following the Loss of Midbrain Dopamine Neurons.* Cell Rep, 2019. **28**(4): p. 992-1002 e4.

115. Mink, J.W. and W.T. Thach, *Preferential relation of pallidal neurons to ballistic movements.* Brain Res, 1987. **417**(2): p. 393-8.

116. Nambu, A., S. Yoshida, and K. Jinnai, *Discharge patterns of pallidal neurons with input from various cortical areas during movement in the monkey.* Brain Res, 1990. **519**(1-2): p. 183-91.

117. Filion, M., L. Tremblay, and P.J. Bedard, *Abnormal influences of passive limb movement on the activity of globus pallidus neurons in parkinsonian monkeys.* Brain Res, 1988. **444**(1): p. 165-76.

bioRxiv preprint doi: https://doi.org/10.1101/2020.02.14.950006; this version posted February 15, 2020. The copyright holder for this preprint (which was not certified by peer review) is the author/funder. All rights reserved. No reuse allowed without permission.

118. Mushiake, H. and P.L. Strick, *Pallidal neuron activity during sequential arm movements.* J Neurophysiol, 1995. **74**(6): p. 2754-8.

119. Arkadir, D., et al., *Independent coding of movement direction and reward prediction by single pallidal neurons.* J Neurosci, 2004. **24**(45): p. 10047-56.

120. Shin, S. and M.A. Sommer, *Activity of neurons in monkey globus pallidus during oculomotor behavior compared with that in substantia nigra pars reticulata.* J Neurophysiol, 2010. **103**(4): p. 1874-87.

121. Mallet, N., et al., *Arkypallidal Cells Send a Stop Signal to Striatum.* Neuron, 2016. **89**(2): p. 308-16.

122. Aron, A.R., et al., *Converging evidence for a fronto-basal-ganglia network for inhibitory control of action and cognition.* J Neurosci, 2007. **27**(44): p. 11860-4.

123. Nambu, A. and R. Llinas, *Morphology of globus pallidus neurons: its correlation with electrophysiology in guinea pig brain slices.* J Comp Neurol, 1997. **377**(1): p. 85-94.

124. Kita, H., *Parvalbumin-immunopositive neurons in rat globus pallidus: a light and electron microscopic study.* Brain Res, 1994. **657**(1-2): p. 31-41.

125. Saunders, A., et al., *A direct GABAergic output from the basal ganglia to frontal cortex.* Nature, 2015. **521**(7550): p. 85-9.

126. Mink, J.W., *The basal ganglia: focused selection and inhibition of competing motor programs.* Prog Neurobiol, 1996. **50**(4): p. 381-425.

127. Klaus, A., et al., *The Spatiotemporal Organization of the Striatum Encodes Action Space.* Neuron, 2017. **95**(5): p. 1171-1180 e7.

128. Arber, S. and R.M. Costa, *Connecting neuronal circuits for movement.* Science, 2018. **360**(6396): p. 1403-1404.

129. Isoda, M. and O. Hikosaka, *Role for subthalamic nucleus neurons in switching from automatic to controlled eye movement.* J Neurosci, 2008. **28**(28): p. 7209-18.

130. Nambu, A., et al., *Excitatory cortical inputs to pallidal neurons via the subthalamic nucleus in the monkey.* J Neurophysiol, 2000. **84**(1): p. 289-300.

131. Kovaleski, R.F., et al., *Dysregulation of external globus pallidus-subthalamic nucleus network dynamics in Parkinsonian mice.* bioRxiv, 2019: p. 774091.

bioRxiv preprint doi: https://doi.org/10.1101/2020.02.14.950006; this version posted February 15, 2020. The copyright holder for this preprint (which was not certified by peer review) is the author/funder. All rights reserved. No reuse allowed without permission.

132. Kita, H. and T. Kita, *Cortical stimulation evokes abnormal responses in the dopamine-depleted rat basal ganglia.* J Neurosci, 2011. **31**(28): p. 10311-22.

133. Smith, Y. and T. Wichmann, *The cortico-pallidal projection: an additional route for cortical regulation of the basal ganglia circuitry.* Mov Disord, 2015. **30**(3): p. 293-5.

134. Cui, Q., et al., *Blunted mGluR Activation Disinhibits Striatopallidal Transmission in Parkinsonian Mice.* Cell Rep, 2016. **17**(9): p. 2431-2444.

135. Bevan, M.D., et al., *Move to the rhythm: oscillations in the subthalamic nucleus-external globus pallidus network.* Trends Neurosci, 2002. **25**(10): p. 525-31.

136. Gillies, A., D. Willshaw, and Z. Li, *Subthalamic-pallidal interactions are critical in determining normal and abnormal functioning of the basal ganglia.* Proc Biol Sci, 2002. **269**(1491): p. 545-51.

137. Terman, D., et al., *Activity patterns in a model for the subthalamopallidal network of the basal ganglia.* J Neurosci, 2002. **22**(7): p. 2963-76.

138. Holgado, A.J., J.R. Terry, and R. Bogacz, *Conditions for the generation of beta oscillations in the subthalamic nucleus-globus pallidus network.* J Neurosci, 2010. **30**(37): p. 12340-52.

139. Hammond, C., H. Bergman, and P. Brown, *Pathological synchronization in Parkinson's disease: networks, models and treatments.* Trends Neurosci, 2007. **30**(7): p. 357-64.

140. Fan, K.Y., et al., *Proliferation of external globus pallidus-subthalamic nucleus synapses following degeneration of midbrain dopamine neurons.* J Neurosci, 2012. **32**(40): p. 13718-28.

141. Chu, H.Y., et al., *Heterosynaptic regulation of external globus pallidus inputs to the subthalamic nucleus by the motor cortex.* Neuron, 2015. **85**(2): p. 364-76.

142. Wilson, C.J. and M.D. Bevan, *Intrinsic dynamics and synaptic inputs control the activity patterns of subthalamic nucleus neurons in health and in Parkinson's disease.* Neuroscience, 2011. **198**: p. 54-68.

bioRxiv preprint doi: https://doi.org/10.1101/2020.02.14.950006; this version posted February 15, 2020. The copyright holder for this preprint (which was not certified by peer review) is the author/funder. All rights reserved. No reuse allowed without permission.

Figure Legends

Figure 1. PV$^+$ neuron activity promotes locomotion.

a. Open field activity in response to optogenetic stimulation of PV$^+$ neurons in the GPe. Top, left: A representative example of the locomotion activity of a single mouse across four individual trials. The schematic diagram shows the cell type and site of light delivery. Blue box indicates the duration (10 s) of light delivery. Top, middle: Movement tracks corresponding to the pre (top) and light (bottom) periods. 10 trials from 6 mice are presented. Top, right: The median difference is plotted on a floating axis as a bootstrap distribution. The median difference is depicted as a circle and the 95% confidence interval is indicated by the ends of vertical error bars. Bottom, left: A plot showing the relationship between normalized distance traveled across time. Blue box indicates the duration (10 s) of light delivery. The dotted horizontal line indicates the normalized baseline motor activity level. Black trace is the mean distance from all mice; the shaded area shows the standard error of the mean (SEM). Bottom, middle: Velocity during light delivery against velocity at pre. Data from PV-Cre mice injected in the GPe with CreOn AAVs for ChR2-eYFP (black) and eYFP (gray) are displayed. Each marker indicates a mouse. The dotted diagonal line indicates unity (i.e., no effect line). Bottom, right: A plot showing the fold change in activity against velocity immediately before light. The dotted line indicates no change in activity. Each marker indicates a mouse. **b.** Open field activity in response to optogenetic stimulation of PV$^+$ neuron terminals in the STN. Left: A plot showing the relationship between normalized distance traveled across time. Middle: Velocity during light delivery against velocity at pre. Right: A plot showing the fold change in activity against velocity right before light delivery. Right, inset: Movement tracks corresponding to the pre (left) or light (right) period of trials from 6 mice. **c.** Open field activity of mice in response to optogenetic inhibition of STN neurons. Left: A plot showing the relationship between normalized distance traveled across time. Middle: Velocity during light delivery against velocity at pre. Right: A plot showing the fold change in activity against velocity right before light delivery. Right, inset: Movement tracks corresponding to the pre (left) or light (right) period. 10 trials from 6 mice are presented.

bioRxiv preprint doi: https://doi.org/10.1101/2020.02.14.950006; this version posted February 15, 2020. The copyright holder for this preprint (which was not certified by peer review) is the author/funder. All rights reserved. No reuse allowed without permission.

Figure 2. Npas1$^+$ neuron activity suppresses locomotion.

a. Open field activity in response to optogenetic stimulation of Npas1$^+$ neurons in the GPe. Top, left: A representative example of locomotion activity of a single mouse across four individual trials. The schematic diagram shows the cell type and site of light delivery. Blue box indicates the 10 s duration of light delivery. Top, middle: Movement tracks corresponding to the pre (top) or light (bottom) period. 10 trials from 6 mice are presented. Top, right: The median difference is plotted on a floating axis as a bootstrap distribution. The median difference is depicted as a circle and the 95% confidence interval is indicated by the ends of vertical error bars. Bottom, left: A plot showing the relationship between normalized distance traveled across time. Blue box indicates the duration (10s) of light delivery. The dotted horizontal line indicates the normalized baseline motor activity level. Black trace is the mean distance from all mice; the shaded area shows the SEM. Bottom, middle: Velocity during light delivery against velocity at pre. Data from Npas1-Cre-tdTom mice injected in the GPe with CreOn AAVs for ChR2-eYFP (black) and eYFP (gray) are displayed. Each marker indicates a mouse. The dotted diagonal line indicates unity (i.e., no effect line). Bottom, right: A plot showing the fold change in activity against velocity right before light delivery. The dotted line indicates no change in activity. Each marker indicates a mouse.

b. Open field activity in response to optogenetic inhibition of Npas1$^+$ neurons. Left: A plot showing the relationship between normalized distance traveled across time. Middle: Velocity during light delivery against velocity at pre. Right: A plot showing the fold change in activity against velocity right before light delivery. Right, inset: Movement tracks corresponding to the pre (left) or light (right) period. 10 trials from 6 mice are presented.

c. Open field activity in response to optogenetic stimulation of Npas1$^+$ neuron terminals in the dorsal striatum (dStr). Left: A plot showing the relationship between normalized distance traveled across time. Middle: Velocity during light delivery against velocity at pre. Right: A plot showing the fold change in activity against velocity right before light delivery. Right, inset: Movement tracks corresponding to the pre (left) or light (right) period. 10 trials from 6 mice are presented.

bioRxiv preprint doi: https://doi.org/10.1101/2020.02.14.950006; this version posted February 15, 2020. The copyright holder for this preprint (which was not certified by peer review) is the author/funder. All rights reserved. No reuse allowed without permission.

Figure 3. STN input is stronger to PV$^+$ neurons than Npas1$^+$ neurons.

a. A confocal micrograph of a sagittal brain section showing eYFP-labeled STN axons in the GPe (in a mouse injected with a ChR2-eYFP AAV in the STN). dStr, dorsal striatum; ic, internal capsule. Inset, high magnification confocal micrograph showing the spatial relationship between eYFP-labeled STN axons (green) and VGluT2 (magenta) labeling. **b.** Left, a schematic showing viral spread overlaid for each subject used for *ex vivo* experiments. Inset: a representative epifluorescent image of a parasagittal acute brain slice showing the expression of Ch2-eYFP in the STN and the neighboring areas. **c.** Left, a brightfield image of a parasagittal acute brain slice showing STN and ZI. Right, eYFP signal from the same slice showing infection only in the ZI but not the STN. **d.** Excitatory postsynaptic currents (EPSCs) recorded in PV$^+$ neurons and Npas1$^+$ neurons in mice that had well-targeted (STN + ZI) and mistargeted (ZI only) infections. Inset: Epifluorescence image from ex vivo tissue showing the GPe of a PV-L-tdTom mouse with tdTomato+ (PV$^+$) and tdTomato$^-$ (PV$^-$) neurons within the same field. **e.** Box plots summarizing the amplitude of excitatory postsynaptic currents (EPSCs) recorded in PV$^+$ neurons and Npas1$^+$ neurons with optogenetic stimulation of terminals from the subthalamic nucleus (STN), the parafascicular nucleus of the thalamus (PF Thal), or the pedunculopontine nucleus (PPN). **f.** Top: a montage of confocal micrographs from a sagittal brain section in a mouse injected with AAV$_{retro}$-Cre in the SNr, along with CreOn ChR2-eYFP-expressing AAVs in the STN. These images show that eYFP-labeled STN axons arborized throughout the GPe and SNr. Bottom: High magnification images showing eYFP-labeled neurons in the STN (left) and their axons in the GPe (right). **g.** Left: CreOn expression of ChR2-eYFP in the STN (top), where eYFP-labeling (bottom) is localized within the STN. Right: Representative EPSC recordings from a voltage-clamped PV$^+$ neuron (top) and a PV$^-$ neuron (bottom) in mice with constitutive (left) or CreOn (right) expression of ChR2-eYFP in the STN. Abbreviations: dStr, dorsal striatum; GPe, external globus pallidus; STN, subthalamic nucleus; SNr, substantia pars reticulata; Thal, thalamus; ZI, zona incerta. Asterisks denote significance: **** for $P < 0.0001$.

bioRxiv preprint doi: https://doi.org/10.1101/2020.02.14.950006; this version posted February 15, 2020. The copyright holder for this preprint (which was not certified by peer review) is the author/funder. All rights reserved. No reuse allowed without permission.

Figure 4. STN-GPe input is weakened following chronic 6-OHDA lesion.

a. Left: Representative voltage-clamped recordings of a PV^+ neuron (top) and a $Npas1^+$ neuron (bottom) in naïve mice (black) showing that optogenetic stimulation of STN terminals evoked EPSCs. Middle: Application of CPP (10 μM) and NBQX (5 μM) completely eliminated the evoked EPSCs. Right: Representative EPSC recordings from a voltage-clamped PV^+ neuron and a $Npas1^+$ neuron in a chronic 6-OHDA lesioned mouse (red) showing a selective reduction in STN input to PV^+ neuron. **b.** Population data showing EPSC amplitudes measured from PV^+ neurons and $Npas1^+$ neurons. Data from naïve (black) and chronic 6-OHDA lesion (red) mice are shown. **c.** Left: EPSC amplitudes of PV^+ neurons (top) or $Npas1^+$ neurons (bottom) were plotted against limb use ratio, which provides a measure of the extent of the lesion. Each marker indicates a cell. Right: Input-output curves from EPSCs measured from PV^+ neurons (top) and $Npas1^+$ neurons (bottom). Each circle represents the mean EPSCs measured at a particular light intensity and the shaded area indicates SEM. **d.** Top: EPSC amplitude measured from neighboring (within 150 μm apart) PV^+ neurons and PV^- neurons in naïve (black) and chronic 6-OHDA lesion (red) PV-L-tdTom mice. Bottom: EPSC amplitude measured from neighboring $Npas1^+$ neurons and $Npas1^-$ neurons in naïve (black) and chronic 6-OHDA lesion (red) Npas1-Cre-tdTom mice. Each marker represents a pair of positively- and negatively-identified neurons recorded from the same field. The dashed line represents the unity line. **e.** Top: Representative synaptic responses from a voltage-clamped spiny projection neuron (SPN) in the dStr. Corticostriatal (Ctx-Str) EPSCs were evoked with electrical stimulation; stimulus artifacts are not displayed. Neurons were voltage-clamped at –80 mV and +40 mV to measure AMPA and NMDA receptor-dependent current, respectively. Bottom: Population data for AMPA-NMDA ratio in direct pathway spiny projection neurons (dSPNs) and indirect pathway spiny projection neurons (iSPNs). **f.** Representative synaptic responses from a voltage-clamped PV^+ neuron. EPSCs were measured with optogenetic stimulation of STN input. Note the relatively small NMDA current in the STN-PV^+ input. Bottom: Population data for AMPA-NMDA ratio in PV^+ neurons and $Npas1^+$ neurons with stimulation of STN terminals in naïve (black) and chronic 6-OHDA lesion (red) mice. **g.** The relationship between NMDA current and AMPA current in PV^+ neurons (top) and $Npas1^+$ neurons (bottom) (with stimulation of STN input) in naïve (black) and chronic 6-OHDA lesion (red) mice. Each marker represents a cell. Asterisks denote significance: *** for $P < 0.001$, **** for $P < 0.0001$.

bioRxiv preprint doi: https://doi.org/10.1101/2020.02.14.950006; this version posted February 15, 2020. The copyright holder for this preprint (which was not certified by peer review) is the author/funder. All rights reserved. No reuse allowed without permission.

Figure 5. The cell-type specificity of STN-GPe EPSCs is not due to topographical biasing.

a. Top: Population data showing EPSC amplitudes from PV^+ neurons in naïve (black) and chronic 6-OHDA lesion (red) mice. Bottom: Population data showing EPSC amplitudes from $Npas1^+$ neurons in naïve (black) and chronic 6-OHDA lesion (red) mice. **b.** EPSC amplitudes measured in PV^+ neurons or $Npas1^+$ neurons represented by the location of the recorded neuron. Data from naïve (black) and chronic 6-OHDA lesion (red) are shown. **c.** Left: Confocal micrographs showing the GPe in sagittal brain sections of a naïve (top, black) or chronic 6-OHDA lesioned (bottom, red) C57BL/6J mice with ChR2-eYFP-expressing AAVs in the STN. Lateral, intermediate, and medial sections of the GPe are shown. **d.** Analysis of the eYFP signal in naïve (black) and chronic 6-OHDA lesioned (red) mice. The surface area of the GPe (left), percent area covered by the eYFP signal (middle), and the integrated density of the eYFP signal (right) are quantified (see Methods). Asterisks denote significance: * for $P < 0.05$, ** for $P < 0.005$.

Figure 6. PV^+ neuron stimulation lessens hypokinetic symptoms.

a. Top: Representative cell-attached recordings from PV^+ neurons in naïve (left, black) and chronic 6-OHDA lesion (right, red) mice. Raster plots show trials from a single PV^+ neuron, where each raster corresponds to an action potential. Each blue square represents a 2 ms light pulse. Bottom: Representative cell-attached recordings from $Npas1^+$ neurons in naïve (left, black) and 6-OHDA lesion (right, red) mice. **b.** Left: Box plots summarizing the population data are shown. Right: the relationship between EPSC amplitude and spontaneous firing rate of PV^+ neurons (top) and $Npas1^+$ neurons (bottom) are shown. Data from both naïve (black) and chronic 6-OHDA lesion (red) mice are included. **c.** Open field activity in response to optogenetic stimulation of PV^+ neurons in the GPe in chronic 6-OHDA lesion mice. Top, left: A representative example of locomotion activity of a single mouse across four individual trials. The schematic diagram shows the cell type and site of light delivery. "Pre" indicates 10 seconds before light delivery; "post" indicates 10 s after light delivery. Bluebox indicates the duration (10 s) of light delivery. Top, middle: Movement tracks corresponding to the pre (top) or light (bottom) period. 10 trials from 6 mice are presented. Top, right: The median difference is plotted on a

bioRxiv preprint doi: https://doi.org/10.1101/2020.02.14.950006; this version posted February 15, 2020. The copyright holder for this preprint (which was not certified by peer review) is the author/funder. All rights reserved. No reuse allowed without permission.

floating axis as a bootstrap distribution. The median difference is depicted as a circle and the 95% confidence interval is indicated by the ends of vertical error bars. Bottom, left: A plot showing the relationship between normalized distance traveled across time. Blue box indicates the duration (10 s) of light delivery. The dotted horizontal line indicates the normalized baseline motor activity level. Black trace is the average distance from all mice; the shaded area shows the SEM. Bottom, middle: Velocity during light delivery against velocity at pre. Each marker indicates a mouse. The dotted diagonal line indicates unity (i.e., no effect line). Bottom, right: A plot showing the fold change in activity against velocity right before light delivery. The dotted line indicates no change in activity. Each marker indicates a mouse. Asterisks denote significance: * for $P < 0.05$, **** for $P < 0.0001$.

bioRxiv preprint doi: https://doi.org/10.1101/2020.02.14.950006; this version posted February 15, 2020. The copyright holder for this preprint (which was not certified by peer review) is the author/funder. All rights reserved. No reuse allowed without permission.

Table 1. Detailed information on viral injections

Viral vector	Source	Working titer (viral genome/ml)
AAV_9.EF1a.DIO.hChR2(H134R).eYFP	Addgene, 20298	5.55E+12 (GPe) 2.00E+12 (STN)
AAV_9.EF1a.DIO.eYFP	Virovek	5.55E+12
AAV_1.CKIIa.stGtACR2.FusionRed	Addgene, 105669	3.00E+11
AAV_1.hSyn1.SIO.stGtACR2.FusionRed	Addgene, 105677	5.00E+11
AAV_9.Syn.ChR2(H134R).eYFP	Addgene, 26973P	2.68E+12
AAV_{retro}.Syn.Cre	Janelia	2.30E+11

Table 2. Viral and 6-OHDA* injection coordinates

Region	Volume (per hemisphere)	Rostral to bregma (mm)	Lateral to bregma (mm)	Ventral to the skull (mm)
GPe	90 nl	−0.28	2.10	4.00
STN	45 nl	−1.70	1.60	4.50
SNr	90 nl	−3.00	1.60	4.20
dStr	720 nl	0.90	1.40	3.20, 3.60
PPN	90 nl	−4.50	1.25	3.50
PF Thal	90 nl	−2.22	0.64	3.20
MFB*	990 nl*	−0.70	1.10	4.95

925

bioRxiv preprint doi: https://doi.org/10.1101/2020.02.14.950006; this version posted February 15, 2020. The copyright holder for this preprint (which was not certified by peer review) is the author/funder. All rights reserved. No reuse allowed without permission.

Table 3. Implantation coordinates

Region	Rostral to bregma (mm)	Lateral to bregma (mm)	Ventral to the skull (mm)
GPe	−0.28	2.1	3.8
STN	−1.70	1.6	4.3
SNr	−3.00	1.6	4.1
dStr	0.90	1.4	3.0

bioRxiv preprint doi: https://doi.org/10.1101/2020.02.14.950006; this version posted February 15, 2020. The copyright holder for this preprint (which was not certified by peer review) is the author/funder. All rights reserved. No reuse allowed without permission.

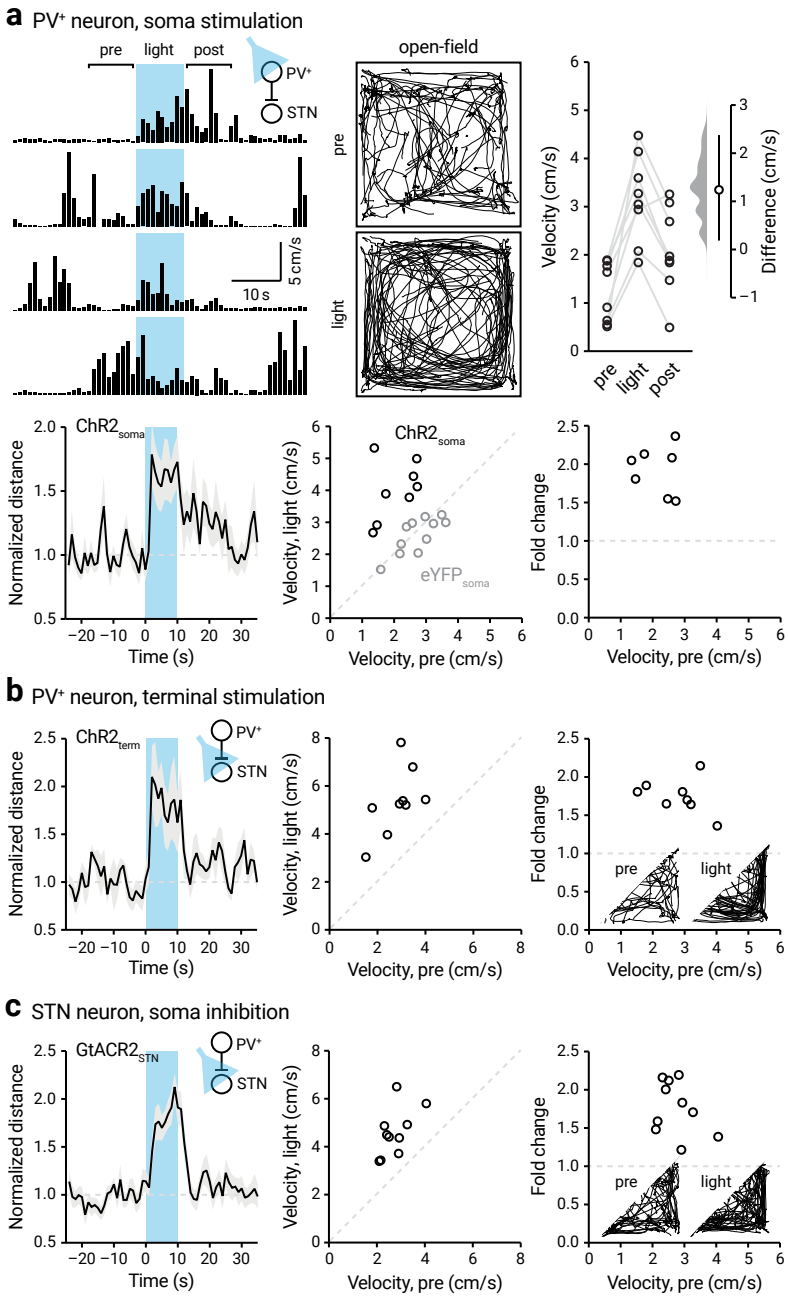

Figure 1

bioRxiv preprint doi: https://doi.org/10.1101/2020.02.14.950006; this version posted February 15, 2020. The copyright holder for this preprint (which was not certified by peer review) is the author/funder. All rights reserved. No reuse allowed without permission.

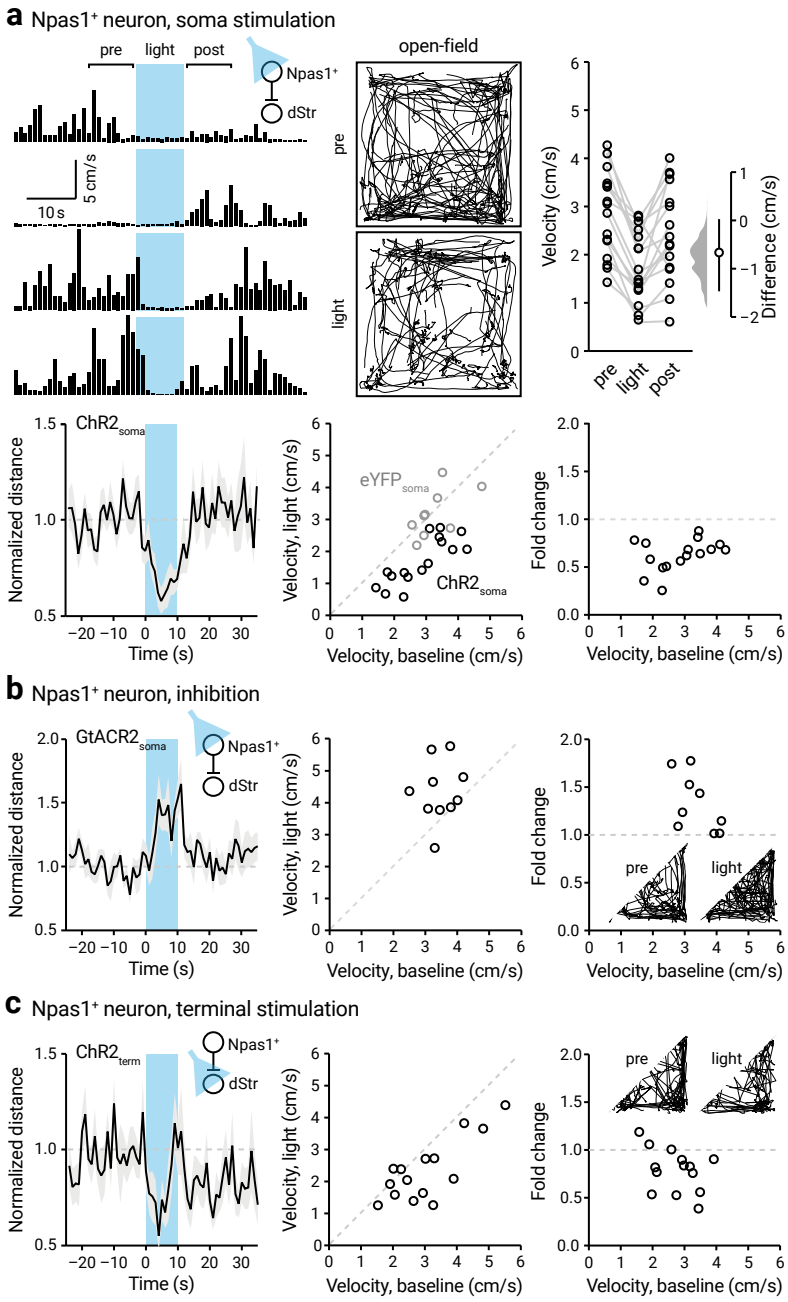

Figure 2

bioRxiv preprint doi: https://doi.org/10.1101/2020.02.14.950006; this version posted February 15, 2020. The copyright holder for this preprint (which was not certified by peer review) is the author/funder. All rights reserved. No reuse allowed without permission.

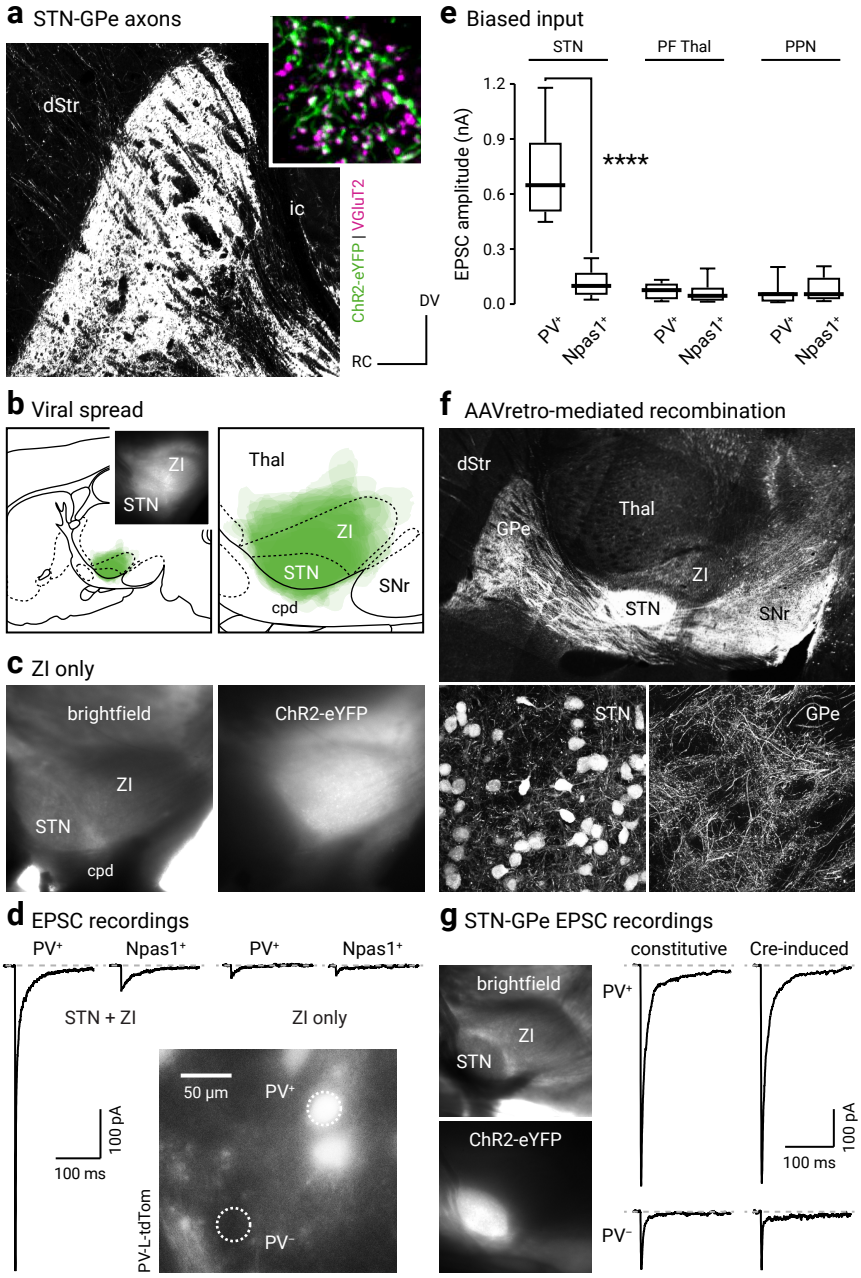

Figure 3

bioRxiv preprint doi: https://doi.org/10.1101/2020.02.14.950006; this version posted February 15, 2020. The copyright holder for this preprint (which was not certified by peer review) is the author/funder. All rights reserved. No reuse allowed without permission.

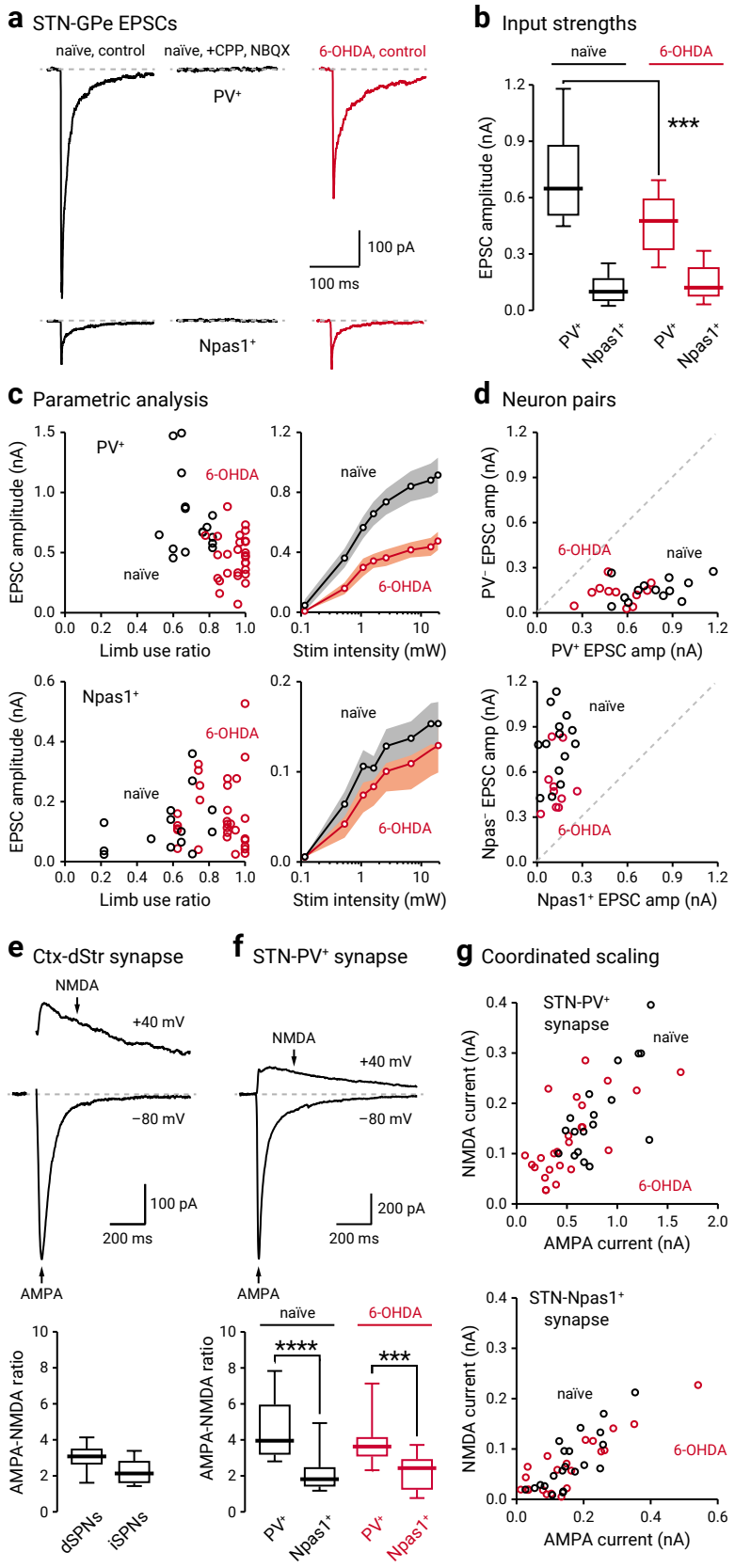

Figure 4

bioRxiv preprint doi: https://doi.org/10.1101/2020.02.14.950006; this version posted February 15, 2020. The copyright holder for this preprint (which was not certified by peer review) is the author/funder. All rights reserved. No reuse allowed without permission.

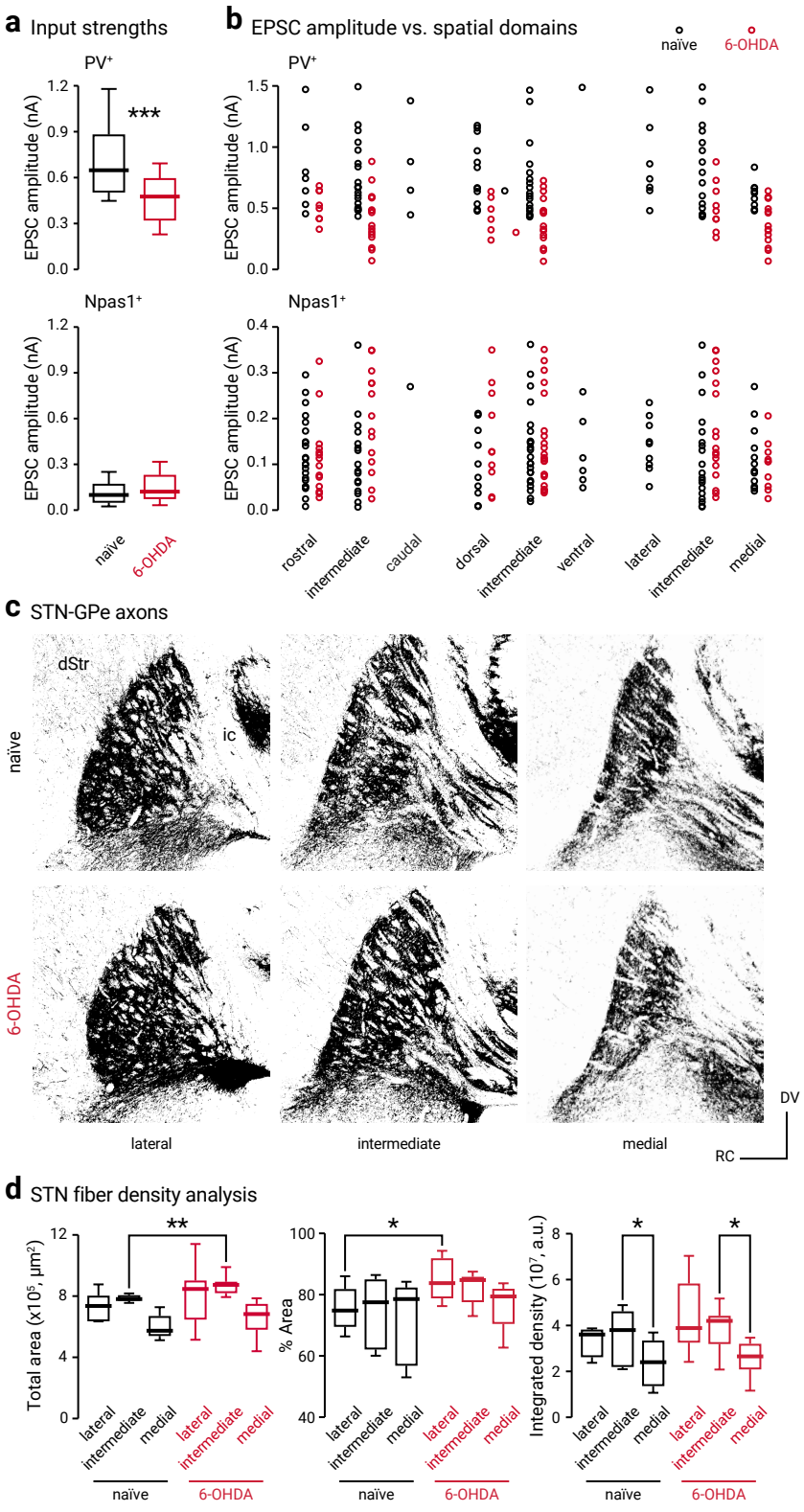

Figure 5

bioRxiv preprint doi: https://doi.org/10.1101/2020.02.14.950006; this version posted February 15, 2020. The copyright holder for this preprint (which was not certified by peer review) is the author/funder. All rights reserved. No reuse allowed without permission.

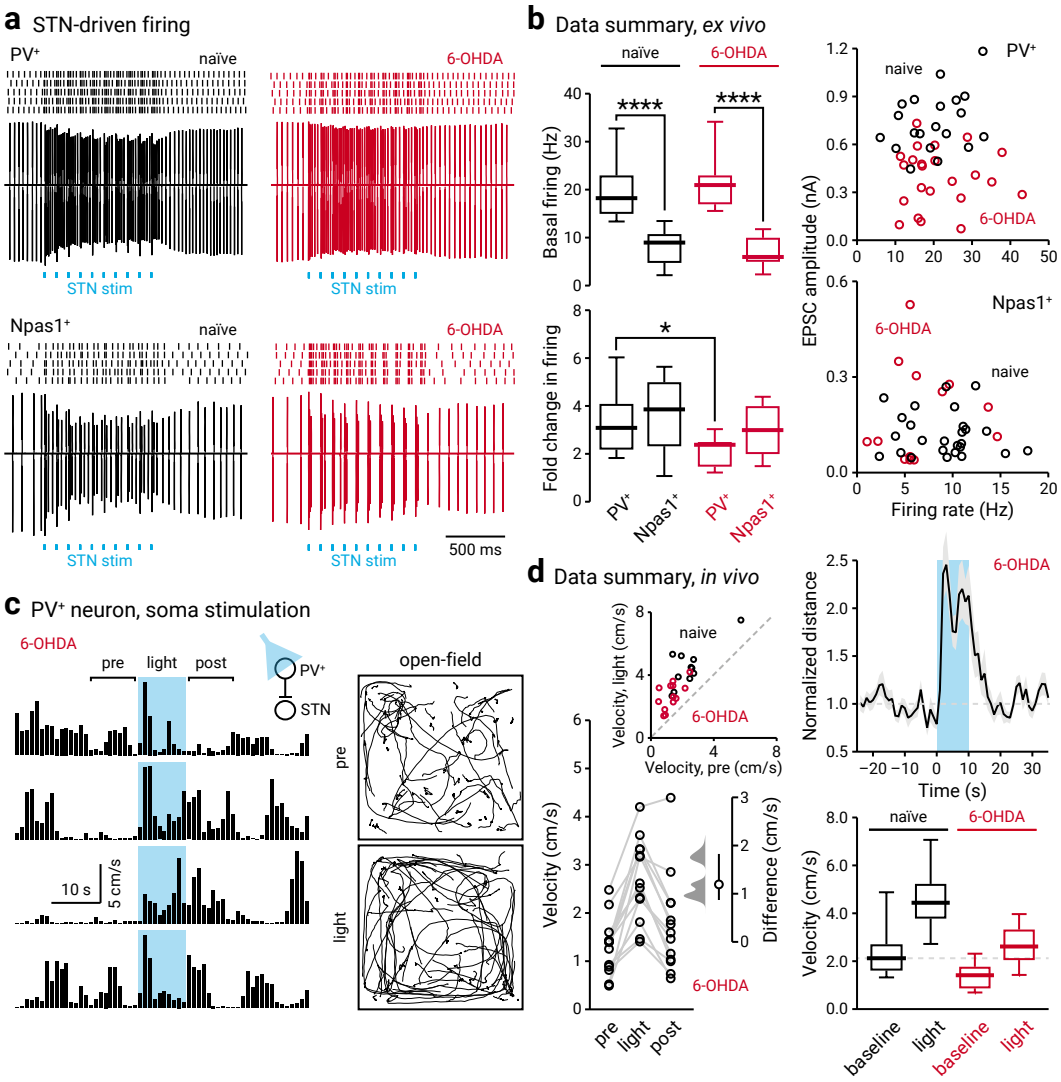

Figure 6